

Constraining global marine iron source and scavenging fluxes with GEOTRACES dissolved iron measurements in an ocean biogeochemical model

Christopher J. Somes^{1,1}, Andrew W. Dale^{2,2}, Klaus Wallmann^{2,2}, Florian Scholz^{1,1}, Wanxuan Yao^{1,1}, Andreas Oschlies^{3,3}, Juan Muglia^{4,4}, Andreas Schmittner^{5,5}, and Eric P. Achterberg^{2,2}

¹GEOMAR Helmholtz Centre for Ocean Research

²GEOMAR Helmholtz Centre for Ocean Research Kiel

³Helmholtz-Zentrum für Ozeanforschung Kiel, GEOMAR

⁴Centro para el Estudio de los Sistemas Marinos CONICET

⁵College of Oceanic and Atmospheric Sciences, Oregon State University

November 30, 2022

Abstract

Iron is a key micronutrient controlling phytoplankton growth in vast regions of the global ocean. Despite its importance, uncertainties remain high regarding external iron source fluxes and internal cycling on a global scale. In this study, we used a global dissolved iron dataset, including GEOTRACES measurements, to constrain source and scavenging fluxes in the marine iron component of a global ocean biogeochemical model. Our model simulations tested three key uncertainties: source inputs of atmospheric soluble iron deposition (varying from 1.4 - 3.4 Gmol/yr), reductive sedimentary iron release (14 - 117 Gmol/yr), and compare a variable ligand parameterization to a constant distribution. In each simulation, scavenging rates were adjusted to reproduce the observed global mean iron inventory for consistency. The apparent oxygen utilization term in the variable ligand parameterization significantly improved the model-data misfit, suggesting that heterotrophic bacteria are an important source of ligands to the ocean. Model simulations containing high source fluxes of atmospheric soluble iron deposition (3.4 Gmol/yr) and reductive sedimentary iron release (114 Gmol/yr) further improved the model, which then required high scavenging rates to maintain the observed iron inventory in these high source scenarios. Our model-data analysis suggests that the global marine iron cycle operates with high source fluxes and high scavenging rates, resulting in relatively short surface and global ocean mean residence times of 0.83 and 7.5 years, respectively, which are on the low-end of previous model estimates. Model biases and uncertainties remain high and are discussed to help improve global marine iron cycle models.

1 **Constraining global marine iron source and scavenging fluxes with**
2 **GEOTRACES dissolved iron measurements in an ocean biogeochemical**
3 **model**

4 **Christopher J. Somes¹, Andrew W. Dale¹, Klaus Wallmann¹, Florian Scholz¹, Wanxuan**
5 **Yao¹, Andreas Oschlies¹, Juan Muglia², Andreas Schmittner³, Eric P. Achterberg¹**

6 ¹ GEOMAR Helmholtz Centre for Ocean Research Kiel, 24105 Kiel, Germany

7 ² Centro para el Estudio de los Sistemas Marinos, CONICET, 2915 Boulevard Brown,
8 U9120ACD, Puerto Madryn, Argentina

9 ³ College of Earth, Ocean, and Atmospheric Sciences, Oregon State University, Corvallis,
10 Oregon 97331, USA

11 Corresponding author: Christopher J. Somes (csomes@geomar.de)

12 **Key Points:**

- 13 • Global marine iron model tests varying levels of atmospheric deposition, sedimentary release,
14 ligand distributions and scavenging rates
- 15 • Simulations that best reproduce observations include variable ligands and high rates of
16 atmospheric deposition and sedimentary release
- 17 • Simulations with high iron sources require high scavenging rates resulting in short residence
18 times

19 **Abstract**

20 Iron is a key micronutrient controlling phytoplankton growth in vast regions of the global ocean.
21 Despite its importance, uncertainties remain high regarding external iron source fluxes and
22 internal cycling on a global scale. In this study, we used a global dissolved iron dataset,
23 including GEOTRACES measurements, to constrain source and scavenging fluxes in the marine
24 iron component of a global ocean biogeochemical model. Our model simulations tested three key
25 uncertainties: source inputs of atmospheric soluble iron deposition (varying from 1.4 - 3.4
26 Gmol/yr), reductive sedimentary iron release (14 - 117 Gmol/yr), and compare a variable ligand
27 parameterization to a constant distribution. In each simulation, scavenging rates were adjusted to
28 reproduce the observed global mean iron inventory for consistency. The apparent oxygen
29 utilization term in the variable ligand parameterization significantly improved the model-data
30 misfit, suggesting that heterotrophic bacteria are an important source of ligands to the ocean.
31 Model simulations containing high source fluxes of atmospheric soluble iron deposition (3.4
32 Gmol/yr) and reductive sedimentary iron release (114 Gmol/yr) further improved the model,
33 which then required high scavenging rates to maintain the observed iron inventory in these high
34 source scenarios. Our model-data analysis suggests that the global marine iron cycle operates
35 with high source fluxes and high scavenging rates, resulting in relatively short surface and global
36 ocean mean residence times of 0.83 and 7.5 years, respectively, which are on the low-end of
37 previous model estimates. Model biases and uncertainties remain high and are discussed to help
38 improve global marine iron cycle models.

39 **1 Introduction**

40 Iron is a critical micronutrient limiting primary productivity in vast ocean regions (Boyd
41 and Ellwood, 2010; Tagliabue et al., 2017). Iron limitation is responsible for the development of
42 so-called High Nitrate Low Chlorophyll (HNLC) regions of the Southern Ocean, Subarctic North
43 Pacific, Subarctic North Atlantic, and Eastern Equatorial Pacific (Moore et al., 2013). Since
44 dissolved iron (DFe) in the ocean exists in the picomolar (pM) to nanomolar (nM) concentration
45 range, historical measurements with higher detection limits and contamination issues have
46 hindered a robust global understanding of the marine iron cycle compared to macronutrients
47 (Bruland et al., 2014). However, over the past two decades, in large part due to the
48 GEOTRACES program, considerable progress has been made and reliable intercomparable iron

49 measurements have become available that permit a more synoptic view of the marine iron cycle
50 (Schlitzer et al., 2018).

51 The increasing number of robust iron measurements has sparked recent modeling efforts.
52 However, few observational constraints are provided on a global scale, and the degree of
53 complexity and assumptions on the mechanistic processes implemented in global marine iron
54 models have varied dramatically (e.g., Tagliabue et al. (2016)). For example, there is no
55 consensus on the rates of key source fluxes to the ocean, particularly from atmospheric
56 deposition (Anderson et al., 2016) and sedimentary release (e.g., Elrod et al. (2004); Dale et al.
57 (2015)) that vary between 1.4 - 30 Gmol yr⁻¹ and 0 - 194 Gmol yr⁻¹, respectively, in state-of-the-
58 art marine iron models (Tagliabue et al., 2016). Since uncertainties associated with scavenging
59 and removal of DFe are also high, global marine iron models can tune scavenging rates to
60 reproduce the global iron inventory with large ranges of sources fluxes (Frants et al., 2016).

61 Another key aspect of marine iron models is the representation of ligands which
62 organically bind DFe and thereby prevent it from being scavenged to sinking particulates. Some
63 models still prescribe a globally constant ligand concentration typically at 1 nM, while others
64 account for ligand distributions via a parameterization or directly simulating ligands as a
65 prognostic tracer. Ligands are thought to be produced by microbes as a by-product during the
66 production of organic matter (Gledhill and Buck, 2012), including by heterotrophic siderophores
67 that flourish when systems become iron stressed (Bundy et al., 2018). This has led modelers to
68 predict ligand concentrations by assuming they are produced during the production of organic
69 matter (e.g. Völker & Tagliabue (2015)) or by prescribing a relationship to other organic tracers
70 such as dissolved organic matter and apparent oxygen utilization (e.g., Tagliabue & Völker
71 (2011); Misumi et al. (2013); Pham and Ito (2018)).

72 The uncertainties associated with external source fluxes and scavenging represent key
73 gaps in understanding the marine iron cycle. This hampers accurate estimates of the DFe budget,
74 residence time and, consequently, its sensitivity to environmental perturbations and climate
75 change. While the rapidly increasing amount of DFe measurements is improving our knowledge
76 of the distribution and inventory of dissolved iron in the ocean, constraining external fluxes has
77 proved to be more difficult. As a result, the range of residence times estimated by the current
78 global marine iron cycle models ranges from less than a decade to multiple centuries (Tagliabue

79 et al., 2016), which limits our ability to confidently predict the impact of changes to the marine
80 iron cycle on productivity in a future ocean. Observational estimates fall within a similar range
81 (Johnson et al., 1997), noting that more recent studies estimate much shorter residence times in
82 the upper ocean (~10 days - 4 years) (Croot et al., 2004; Sarthou et al., 2003) depending on the
83 dynamics, iron pools considered, and source inputs in different regions (Black et al., 2020).

84 In this study, we use a global marine DFe dataset to constrain the iron cycle fluxes in a
85 global marine biogeochemical model. We analyze model sensitivity simulations that focus on
86 three key uncertainties: varying source fluxes of (1) atmospheric soluble iron deposition and (2)
87 reductive sedimentary iron release, as well as the role of a (3) variable ligand distribution on DFe
88 distribution and scavenging rates. The resulting DFe concentrations in each model simulation are
89 evaluated against observations to determine the most realistic marine iron cycle fluxes among the
90 model scenarios.

91 **2 Model Description**

92 We used the UVic Earth System Climate Model (Weaver et al., 2001) version 2.9 (Eby et
93 al., 2009). In the following section, we provide a general overview of the model components
94 then focus on improvements made to the marine iron cycle in this study, whereas other
95 modifications applied to all model simulations are described in the supplementary information.

96 **2.1 Physical Model**

97 The physical ocean-atmosphere-sea ice model includes a three-dimensional (1.8x3.6°, 19
98 vertical levels) general circulation model of the ocean (Modular Ocean Model 2) with
99 parameterizations such as diffusive mixing along and across isopycnals and eddy-induced tracer
100 advection (Gent and McWilliams, 1990). The physical configuration is based on Somes et al.
101 (2017) and includes parameterizations such as computation of tidally-induced diapycnal mixing
102 over rough topography on the sub-grid scale (Schmittner and Egbert, 2014), anisotropic viscosity
103 (Large et al., 2001; Somes et al., 2010), and enhanced zonal isopycnal mixing schemes in the
104 tropics to better represent zonal equatorial undercurrents (Getzlaff and Dietze, 2013). A two-
105 dimensional, single level energy-moisture balance atmosphere and a dynamic-thermodynamic
106 sea ice model are used, forced with prescribed monthly climatological winds (Kalnay et al.,
107 1996) and constant ice sheets (Peltier, 2004).

108 **2.2 Marine Biogeochemical Model**

109 The updated marine ecosystem-biogeochemical model coupled within the ocean
110 circulation model is based on the Model of Ocean Biogeochemistry and Isotopes (MOBI),
111 version 2.0. Briefly, MOBI includes three prognostic inorganic nutrient tracers (nitrate (NO_3),
112 phosphate (PO_4), iron) and two organic (dissolved organic nitrogen (DON) and dissolved organic
113 phosphorus (DOP)) phases, three phytoplankton (ordinary, N_2 -fixing diazotrophs, calcifying
114 coccolithophores), one zooplankton, sinking detritus (i.e. dead particulate organic matter
115 (POM)), as well as dissolved oxygen (O_2), dissolved inorganic carbon, alkalinity, and $\Delta^{14}\text{C}$
116 (Figure S1). It combines latest features from previous studies focusing on the nitrogen cycle
117 (Somes and Oschlies, 2015), iron cycle (Muglia et al., 2017), and carbon chemistry (Kvale et al.,
118 2015). Note that MOBI also includes isotope systems of ^{13}C and ^{15}N (Schmittner and Somes,
119 2016), but they are not shown in this study focusing on the iron cycle. Our model experiments
120 were simulated for over 5,000 years under pre-industrial boundary conditions as they approached
121 their quasi steady-state.

122 **2.3 Marine Iron Cycle Model**

123 **2.3.1 Base Configuration**

124 The marine iron model configuration is based on previous UVic Kiel Marine
125 Biogeochemistry Model (KMBM) (Nickelsen et al., 2015), including improvements
126 implemented in Muglia et al. (2017) (Figure 1). The marine iron model includes explicit tracers
127 for DFe and particulate iron (PFe). All phytoplankton grow with a constant elemental
128 stoichiometry ratio of iron relative to nitrogen. The sources of DFe to the ocean are atmospheric
129 soluble deposition (Luo et al., 2008), reductive dissolution and sedimentary release (Elrod et al.,
130 2004; Moore and Braucher, 2008), and hydrothermal fluxes (Tagliabue et al., 2010) (Table 2,
131 Figure 2). The ligand concentration determines the fraction of DFe that is organically complexed
132 and thus unavailable for scavenging, whereas the remaining free DFe (DFe') pool can be
133 scavenged to PFe. In the base simulation #1, ligands are prescribed to be globally constant at 1
134 nM as in previous iterations of the model. This simulation is given the name
135 “*SedFeLow_LigConst*” to reflect its differences (i.e., low reductive sedimentary iron release and
136 constant ligand distribution) from further changes made to the marine iron model in this study
137 (see subsections below and Tables 1 and 2).

138 **2.3.2 Scavenging**

139 The general formulation for scavenging and partitioning of free and organically-
140 complexed DFe remains unchanged from previous versions. Scavenging of DFe' to PFe occurs
141 via two mechanisms in the model: (1) absorption onto particulate organic matter following
142 (Honeyman et al., 1988;Parekh et al., 2004), which is a function of POM concentrations, DFe',
143 and the particle scavenging rate; (2) inorganic scavenging, which depends only on DFe' and the
144 inorganic scavenging rate following the scheme of Galbraith et al. (2010). This inorganic
145 scavenging term primarily represents colloidal aggregation into larger, sinking particles as well
146 as lithogenic scavenging not explicitly accounted for in our formulation. Here we use a non-
147 linear formulation for inorganic scavenging following Galbraith et al. (2010) which was
148 designed to account for high lithogenic scavenging rates to better reproduce DFe where
149 atmospheric deposition is high (e.g., tropical and subtropical North Atlantic) (Pham and Ito,
150 2019;Ye and Völker, 2017).

151 In each model simulation, the scavenging rate parameters were tuned so that each
152 simulation contains a nearly identical global iron inventory with an average global DFe
153 concentration of 0.7 ± 0.03 nM (Table 2). The inorganic scavenging term was adjusted to
154 reproduce the iron inventory in the ocean interior since it is the dominant form of scavenging
155 there, whereas the POM scavenging parameter was adjusted to the upper ocean DFe. The
156 globally integrated rates of the different scavenging processes are shown in Table 2 and total
157 basin-scale averages in Figure 4.

158 **2.3.3 Ligand Parameterization**

159 In the base model configuration (simulation #1 *SedFeLow_LigConst*), a constant ligand
160 concentration of 1 nM is applied globally (see Table 1). However, the distribution of ligands in
161 the ocean is variable (e.g. Völker and Tagliabue (2015)). Since iron-binding ligands are thought
162 to be produced during the production of organic matter (Gledhill and Buck, 2012), dissolved
163 organic matter (DOM) and apparent oxygen utilization (AOU) have been shown to qualitatively
164 reflect some observed ligand concentration patterns (Misumi et al., 2013;Pham and Ito,
165 2018;Tagliabue and Völker, 2011). However, a first global model-data comparison with ligands
166 simulated as prognostic tracers was less conclusive and is further complicated by large variations
167 in binding strength of different types of ligands (Völker and Tagliabue, 2015). Therefore, to

168 maintain computational efficiency we pragmatically chose to implement a ligand concentration
 169 function rather than include additional prognostic tracers.

170 We implemented a variable ligand parameterization to estimate ligand concentrations
 171 based on a function of dissolved organic nitrogen (DON) and apparent oxygen utilization
 172 (AOU): $Ligand_{con} = \alpha \cdot AOU^{0.8} + \beta \cdot DON^{0.8}$, where α (0.015 nmol ligand/(mmol AOU m⁻³)^{0.8}) and
 173 β (0.21 nmol ligand/(mmol DON m⁻³)^{0.8}) are generic parameters that determine ligand
 174 concentration associated with the tracers AOU and DON, respectively. The parameters α and β
 175 were chosen so that the global ligand inventory remained at 1 nM consistent with *LigConst*
 176 simulations but now reflects changes in their spatial distribution (Figure 3). Model simulations
 177 with this variable ligand parameterization (simulations #2-5, see Table 1) have “*LigVar*” in their
 178 respective model simulation name.

179 Although we follow previous studies for the variable ligand parameterization (Misumi et
 180 al., 2013;Pham and Ito, 2018;Tagliabue and Völker, 2011), a few notable changes have been
 181 made in our version. Since AOU can be negative in the surface ocean due to dissolved oxygen
 182 supersaturation, we applied a minimum ligand concentration of 0.5 nM. Previous ligand
 183 parameterizations have also applied minimum ligand concentrations to account for ligands
 184 associated with more refractory forms of DOM not explicitly included in our model (Aumont et
 185 al., 2015;Tagliabue and Völker, 2011). We also applied an exponential parameter (0.8) to the
 186 AOU and DON terms, which reduces ligands associated to these tracers particularly when their
 187 concentrations are high. This helped the model from overestimating DFe concentrations when
 188 AOU and DON concentrations are at their highest concentrations in the model.

189 **2.3.2 Reductive Sedimentary Iron Release Function**

190 The base model version uses reductive sedimentary iron release based on the Moore and
 191 Braucher (2008) implementation of Elrod et al. (2004), $DFe_{sed} = \gamma_{FeSed} \cdot C_{ox}$, where the DFe flux
 192 from the sediments (DFe_{sed}) is determined by the sedimentary iron release rate ($\gamma_{FeSed} = 0.27$
 193 $\mu\text{mol Fe mmol } C_{ox}^{-1} \text{ m}^{-2} \text{ d}^{-1}$), and organic carbon oxidation (C_{ox}) in the sediments. Note that the
 194 base model version uses the DFe flux rate from Nickelsen et al. (2015) that is lower than
 195 suggested by Elrod et al. (2004) ($0.72 \mu\text{mol Fe mmol } C_{ox}^{-1} \text{ m}^{-2} \text{ d}^{-1}$). Since this formulation yields
 196 lower global rates in the model compared with other implemented sedimentary functions

197 included in this study (described below), model simulations with this sedimentary iron function
198 (#1-2) contain the name “*SedFeLow*”.

199 We also implemented the sedimentary iron release function proposed by Dale et al.
200 (2015), who compiled a global dataset of sedimentary DFe fluxes to constrain their model
201 estimate. While it has a strong dependence on the flux of particulate organic matter to the
202 seafloor, similar to Elrod et al. (2004), the dataset in Dale et al. (2015) also revealed a strong
203 dependence on bottom water oxygen concentration. Dale et al. (2015) thus parameterized
204 sedimentary DFe release as $DFe_{sed} = \gamma_{max} \cdot \tanh(C_{ox}/bwO_2)$, where γ_{max} is the maximum flux under
205 steady-state conditions, and bwO_2 is dissolved oxygen concentration in bottom waters interacting
206 with the sediments.

207 We test two scenarios with the Dale et al. (2015) parameterization by altering the
208 maximum flux under steady-state conditions parameter. The “*SedFeHigh*” simulations apply the
209 value suggested by Dale et al. (2015) ($\gamma_{max} = 170 \mu\text{mol m}^{-2} \text{d}^{-1}$), whereas the “*SedFeMid*”
210 simulation reduces the maximum steady-state flux value to $100 \mu\text{mol m}^{-2} \text{d}^{-1}$ to test more
211 intermediate levels of sedimentary DFe release (see Tables 1 and 2). This reduced value was
212 chosen to test a global sedimentary DFe flux approximately halfway in between *SedFeHigh* and
213 *SedFeLow* since their fluxes differ by a large amount. Note that the *SedFeMid* simulation does
214 not contain significant qualitative differences in its spatial distribution compared to *SedFeHigh*.

215 **2.3.4 Atmospheric Soluble Iron Deposition**

216 In the base configuration, we applied the atmospheric soluble iron deposition mask from
217 Luo et al. (2008). It deposits 1.4 Gmol yr^{-1} of soluble iron to the global ocean, which is a low-
218 end scenario compared to other estimates applied in the marine iron model intercomparison
219 study (Tagliabue et al., 2016). This estimate from Luo et al. (2008) is one of the first deposition
220 models that explicitly accounts for the soluble iron deposition rather than assuming a constant
221 solubility percentage from total deposition.

222 Another scenario using the average flux from four recent atmospheric soluble iron
223 deposition models has also been applied (Myriokefalitakis et al., 2018). The intermodel average
224 global soluble deposition rate is 3.4 Gmol yr^{-1} with similar patterns as in Luo et al. (2008) but
225 higher rates most notably in the North Atlantic (Figure 2). This simulation with high soluble

226 atmospheric iron deposition is only applied to the high sedimentary release scenario and is
227 therefore named “*Atm+SedFeHigh_LigVar*”.

228 **3 Model Results and Data Comparison**

229 **3.1 Global Dissolved Iron Dataset**

230 The DFe database used in this study is a collection of observations from both
231 GEOTRACES Intermediate Data Product 2017 (7520 points; Schlitzer et al. (2018)) and prior
232 observations compiled by Tagliabue et al. (2012) (12371 points). Note that we excluded 37
233 measurements with high DFe concentrations (from 10 nM to 216 nM) mainly from locations
234 with high hydrothermal activities or near-shore settings, and thus the dataset contains
235 concentrations up to 10 nM. We then interpolated the database onto the UVic model grid for the
236 model-data comparison (Figures 3-6) and to calculate model-data statistical metrics (Figure 7),
237 which results in 5917 grid points covered with DFe observations.

238 Model-data misfit statistical metrics are sensitive to unresolved outlier concentrations and
239 spatial extent of the data interpolation onto the model grid. However, these aspects do not affect
240 which simulations best reproduce the global dataset according to statistical metrics. This is
241 illustrated by comparing metrics calculated from all observations (Figure 7 upper panels) to only
242 GEOTRACES (Figure 7 lower panels). The statistical metrics improve when using only
243 GEOTRACES observations (see differences in vertical axes ranges from upper and lower
244 panels), but the relative improvements in the model simulations are nearly identical. The
245 arbitrary threshold of 10 nM was chosen as a balance between including as many observations as
246 possible while still being able to calculate useful statistical metrics.

247 **3.2 Variable Ligand Distribution**

248 The simulation with constant ligands does not reproduce the major basin-scale features of
249 the observed DFe distribution despite that its globally averaged profile is (Figure 4b). Most
250 notably, simulations with constant ligands significantly overestimate the DFe in the interior
251 Southern Ocean (Figure 4k), a critical ocean basin for Fe-limited phytoplankton growth.
252 *LigConst* thus overestimates supply of DFe via upwelling, and underestimates Fe limitation of
253 phytoplankton growth, which is a key deficiency in the base configuration and previous model
254 versions (e.g. Muglia et al. (2017)).

255 The simulations with variable ligand concentrations (#2-5; *LigVar*) better reproduce the
256 ocean interior distribution of DFe. This is due to the AOU dependence of the variable ligand
257 parameterization which mainly determines ligand concentrations in the deep ocean since semi-
258 refractory DOM concentrations are low there in the model. This is most obvious when
259 comparing intermediate depths of the Southern and Indian-Pacific Oceans, which contain
260 relatively low and high values of AOU and thus ligand concentrations, respectively, according to
261 our parameterization (Figures 3,4). Lower ligand concentrations in the Southern Ocean enhances
262 scavenging causing lower DFe concentrations, with the opposite effect occurring in the Indian-
263 Pacific Ocean, and better reproduces observations in both basins. Therefore, the interior DFe
264 distribution with the variable ligand parameterization is better partitioned with respect to
265 observations (Figure 3) and improves the global model-data misfit (Figure 7).

266 The concentration of semi-refractory DOM largely determines ligand concentrations in
267 the surface ocean (Figure 3a). DOM concentrations are higher around the high productivity
268 regimes in the low latitudes with generally decreasing values towards higher latitudes (Somes
269 and Oschlies, 2015) (Figure S2). This pattern is reflected in the surface DFe distribution that
270 shows the same latitudinal trend in the variable ligand model (Figures 5). While this meridional
271 DFe pattern better reproduces low DFe concentrations in the HNLC Southern Ocean, it creates
272 larger model-data biases on high latitude continental shelves in the Bering Sea, Weddell Sea, and
273 European shelf seas (Figures 5a-d, 6b-d). This shows that while the overall variable ligand effect
274 significantly improves the global DFe distribution (Figure 7), model-data biases in some regions
275 (e.g. high latitude continental shelf seas) still increase.

276 **3.3 Sedimentary Iron Release**

277 The *SedFeLow* simulations provide a relatively poor fit to observed DFe concentrations
278 (Figure 7). They fail to reproduce the high DFe concentrations near continental margins (Figures
279 5, 6), suggesting higher sedimentary release rates are necessary to explain these features. The
280 simulated DFe distribution also lacks the strong spatial gradient towards depleted concentrations
281 in many open ocean regions in the observations. These overly smooth gradients in *SedFeLow* are
282 the result of low sedimentary release rates and low scavenging rates required to reproduce the
283 global mean DFe inventory, resulting in a relatively long global mean residence time of 35 years
284 among our simulations (Table 2).

285 The simulations with higher sedimentary release rates (Figure 2) produce higher DFe
286 concentrations in continental shelf seas (Figures 5e-f, 6), particularly where bottom water oxygen
287 is low in the low latitudes. The simulations applying high-end sedimentary Fe release rates
288 (*SedFeHigh*) outperformed simulations assuming lower rates across all calculated statistical
289 metrics (e.g., correlation coefficient, standard deviation, root-mean-squared error; see Figure 7)),
290 with the intermediate release rate scenario *SedFeMid* performed between *SedFeLow* and
291 *SedFeHigh*. Therefore, our model-data analysis suggests that high-end estimates for global
292 reductive sedimentary iron release rates are the most realistic.

293 One region that was notably improved by high sedimentary release rates was the low
294 latitude Pacific (Figure 5e-f, 6a). Observations there in both the eastern (near oxygen deficient
295 zones (ODZs)) and western (Indonesian Shelf Seas) sectors show high DFe concentrations that
296 are best reproduced in *SedFeHigh* scenarios. Since *SedFeHigh* simulations also contain high
297 scavenging rates, they better reproduce the lowest DFe concentrations in the central locations
298 between the continental margins as well.

299 The high DFe concentrations on high latitude continental shelf systems (Figures 5, 6b,d)
300 are not significantly improved in *SedFeHigh* scenario due to the interactions with ligands and
301 scavenging. Lower ligand concentrations in high latitude systems allow scavenging to
302 compensate the additional sediment-derived DFe more efficiently, in contrast to low latitude
303 systems (e.g. Tropical Pacific) that contain higher ligands and allow the DFe to be retained in the
304 water column. Therefore, the model improves but still underestimates DFe in these high latitude
305 continental shelf systems (e.g., Bering Sea and European Shelf Seas).

306 **3.4 Atmospheric Soluble Deposition**

307 The two soluble atmospheric deposition scenarios tested here predict similar spatial
308 depositional patterns (Figure 2), with the more recent GESAMP intermodel average
309 (Myriokefalitakis et al., 2018) providing a significantly higher global deposition rate (3.4 Gmol
310 yr⁻¹) relative to the estimate from Luo et al. (2008) (1.4 Gmol yr⁻¹). These enhanced rates cause
311 higher DFe concentrations mainly from the Saharan dust plume in subtropical North Atlantic, but
312 also to a lesser degree in the Arabian Sea and North Pacific (Figure 5g,h, Figure 6d). The impact
313 of including higher soluble deposition only slightly improves the global model-data statistical

314 metrics, making it difficult to judge the most realistic scenario based on our model-data DFe
315 comparison alone.

316 **3.5 High Scavenging Effect**

317 In model simulations with high source fluxes (e.g. #5 *Atm+SedFeHigh_LigVar*), higher
318 scavenging rates are necessary to maintain a realistic global DFe inventory (Tables 1 and 2).
319 Scavenging is thus more effective at reducing DFe concentrations in the high source flux
320 simulations. In regions far away from the source fluxes, particularly in the deep ocean (Figure 2)
321 and open ocean (e.g. see Figure 5e-h, Figure 6a,b), the model simulations with higher source
322 fluxes actually contain lower dFe because the enhanced scavenging outweighs the source fluxes
323 in these areas. Lower DFe concentrations in these deep and open ocean regions better reproduce
324 observations further improving the model-data misfit metrics (Figure 7).

325 **4 Discussion**

326 **4.1 Model-Data Constraints and Uncertainties**

327 The variable ligand parameterization significantly improved the model's ability to
328 reproduce the distribution of DFe observations in the interior ocean mainly due to AOU
329 dependency of this parameterization. Since ligands are produced when dissolved oxygen is
330 consumed during the respiration of POM via heterotrophic microbes in the variable ligand
331 parameterization, their concentrations reach maximum values in old Pacific intermediate waters
332 (Figure 3), which prevents scavenging causing the model to better reproduce high observed DFe
333 concentrations there (Figure 4h). This model improvement suggests that ligand production by
334 heterotrophic bacteria is a key mechanism maintaining the global marine iron cycle (Misumi et
335 al., 2013;Pham and Ito, 2018).

336 Although not a focus of this study, the model was not able to reproduce the full spatial
337 extent of high DFe concentrations near hydrothermal vents at mid-ocean depths (Figure 4)
338 despite that this source is included (Table 2). Resing et al. (2015) was only able to reproduce this
339 DFe extent when assuming that the hydrothermal vents were also a significant source of ligands.
340 This emphasizes that future model versions should include ligands as prognostic tracers to more
341 mechanistically represent their importance in marine iron models, but that a more robust global

342 database of ligand concentrations including their binding strength would be required (Völker and
343 Tagliabue, 2015).

344 The ligand and high sedimentary DFe release effects have similar spatial impacts on DFe
345 concentrations making it difficult to constrain their individual impacts with DFe concentrations
346 alone. This spatial overlap is most pronounced near ODZs in the eastern tropical Pacific, eastern
347 tropical Atlantic, and Northern Indian Ocean. This spatial covariance occurs because when AOU
348 is high, bottom water oxygen is typically low. Therefore, DFe concentrations are enhanced both
349 by reduced scavenging due to high ligands where AOU is high as well as high sedimentary DFe
350 release rates where bottom water oxygen is low. Future studies should examine the integrative
351 DFe cycling in these systems (e.g. sedimentary release rates and ligand concentrations) to give
352 additional insights on individual processes contributions to total DFe.

353 Despite high sedimentary release rates, the *SedFeHigh* model simulations still
354 underestimate DFe on most continental shelf systems. The poorly resolved coastal dynamics in
355 our coarse resolution circulation model is likely a key model deficiency preventing the model
356 from representing many coastal dynamics where sedimentary DFe fluxes are high. Coarse
357 resolution models underestimate coastal upwelling and the nutrient input on narrow shelf
358 systems that drive productivity. This bias causes underestimated particulate organic matter
359 production as well as overestimated dissolved bottom water oxygen concentrations, both of
360 which would contribute to underestimating reductive sedimentary DFe release rates and from
361 coastal shelf systems.

362 Further complicating matters are interactions between sedimentary DFe release fluxes,
363 ligands, and scavenging. For example, our *SedFeHigh* model simulation releases significantly
364 higher DFe on high latitude shelves (Figure 2e-f). However, only a small part of this DFe
365 remains in the dissolved pool since scavenging efficiently converts it to particulate iron that
366 eventually sinks back to the sediments. Therefore, our model underestimation of DFe
367 concentrations remains despite high DFe release rates. Underestimated organic matter due to
368 nutrient upwelling or the exclusion of riverine inputs which may include ligands could also
369 contribute to this model bias. If our ligand parameterization predicted higher concentrations on
370 these high latitude shelf systems, which has been indicated by ligand observations (Völker and

371 Tagliabue, 2015), this would prevent rapid scavenging of DFe released from sediments and
372 better reproduce observations.

373 Sedimentary DFe release rates may still be underestimated even in our high release
374 scenario. Note that our highest tested global sedimentary release rate (117 Gmol yr^{-1}) was not the
375 highest from the marine iron mode intercomparison (up to 194 Gmol yr^{-1}) (Tagliabue et al.,
376 2016), and every model scenario tested here with increased source fluxes improved the model-
377 data misfit metrics (Figure 7). One potentially important process not included in the model is
378 non-reductive dissolution from young, tectonically active sediments (Conway and John,
379 2014; Homoky et al., 2013), which could further contribute to higher total sedimentary DFe
380 release rates that may improve the model.

381 An important limitation of applying these empirical functions of sedimentary DFe release
382 (e.g. (Dale et al., 2015; Elrod et al., 2004)) in global models is that total iron balance within the
383 sediments is not explicitly accounted for. Thus, these parameterizations can potentially represent
384 an infinite source of DFe to the ocean which is unrealistic. This simplification can be justified
385 because many important sources of particulate Fe to the sediment are not yet included in the
386 model, e.g. atmospheric and riverine input of lithogenic material and in situ production in active
387 margins (e.g. volcanic or subduction zones), which provide DFe for release. Also note that the
388 Dale et al. (2015) parameterization applied in the *SedFeHigh* simulations sets a maximum rate
389 determined under steady-state conditions which caps potentially unrealistic high release rates.
390 While this simplification is likely not a significant deficiency in steady-state model simulations
391 presented here, this should be considered in transient simulations with substantial enhancement
392 of sedimentary DFe fluxes.

393 Atmospheric deposition often occurs at high rates over continental shelves (e.g. North
394 Pacific, Patagonia) and ODZs (e.g. Arabian Sea), again making it difficult to constrain individual
395 processes driving DFe concentrations when multiple processes act together in close spatial
396 proximity. For example, our high atmospheric soluble deposition scenario helps reproduce high
397 DFe concentrations in the Arabian Sea (Figure 5g,h). However, our model underestimates the
398 extent of the Arabian ODZ which could be the real cause driving high DFe concentrations there
399 via high sedimentary DFe release, reduced scavenging, and/or enhanced redox cycling (Moffett
400 et al., 2007).

401 The model simulations do not resolve the high variance of the observations which is
402 reflected in the underestimated standard deviation model-data misfit metric (i.e. normalized
403 standard deviation values fall below the value one; Figure 7). High variance in the global dataset
404 may not reflect mean climatological conditions simulated by the steady-state model results given
405 the highly dynamic nature of DFe cycling particularly in the surface ocean (Black et al., 2020),
406 and the limitations of spatial and temporal sparsity of the dataset. But note that the standard
407 deviation was significantly improved in our best model simulation with variable ligands and high
408 source/scavenging fluxes (*#5 Atm+SedFeHigh_LigVar*; see Figure 7). Since most DFe
409 observations have been collected in recent decades, there could already be a significant
410 anthropogenic impact (e.g. enhanced deoxygenation, atmospheric pollutant deposition) on the
411 global marine iron cycle not included in these model simulations, especially if the marine DFe
412 residence time operates on decadal timescales or less. Future additions and expansion to the
413 global DFe dataset as well as comparison with transient model simulations at the same period of
414 data collection will improve uncertainties in future model-data analyses.

415 **4.2 A global marine iron cycle with a mean residence time under a decade?**

416 Our model simulations testing various external source fluxes in the global marine iron
417 cycle result in global average residence times ranging from 7.5 to 36 years. The simulation that
418 best reproduces the observations (*#5 Atm+SedFeHigh_LigVar*) has the lowest residence time
419 (global: 7.5 years; surface ocean: 0.83 years) among our model experiments. This low-end
420 residence time is caused in large part due to the high source fluxes, with the reductive
421 sedimentary release being the most important with the highest rate in our simulations. These high
422 source fluxes need to be compensated by efficient scavenging and subsequent removal via burial
423 in the sediments to reproduce the distribution and global mean inventory in DFe observations.

424 This is in general agreement with observational studies focusing on the surface layer
425 (Black et al., 2020; Sarthou et al., 2003). For example, Black et al. (2020) estimated similar
426 residence times throughout the global surface ocean (0-250 meters) for DFe ranging from
427 approximately 1 month to 4 years depending on the region and specific iron pools considered,
428 although noting that the uncertainties remain large (i.e. equal or greater than the absolute value
429 of the estimate in each region). These generally low surface residence times are captured in our
430 model simulations that range from 0.83 to 3.12 years (Table 2). Whereas DFe in the ocean

431 interior is more stable and controlled by the amount of ligands that prevent scavenging and
432 removal to the sediments via sinking particulates, contributing to the longer global mean
433 residence times.

434 **4.3 Marine iron flux impacts on global ocean biogeochemistry**

435 An interesting feature of the model simulations is that there is surprisingly little change to
436 large scale marine productivity, export production, and ODZ volume (Table 3). This occurs in
437 large part in the model because scavenging was also increased in high sedimentary iron release
438 scenarios, and thus much of the additional DFe fluxes from the sediments is efficiently
439 scavenged to particulate iron that sinks back to the sediments before it can be transported to the
440 surface ocean where it may stimulate additional productivity. This general impact was also found
441 in a model study using a previous iteration of the model version used here but comparing
442 different complexities of the marine iron configurations (Yao et al., 2019) rather than source and
443 scavenging fluxes tested here.

444 However, there was a notable increase in dissolved oxygen levels originating in the
445 Southern Ocean among our model simulations (Table 3). The variable ligand parameterization
446 predicts less ligands in the Southern Ocean (Figure 3), which allows higher scavenging to reduce
447 DFe that better reproduces observations. Furthermore, since external iron sources in the Southern
448 Ocean are small (Figure 2,4j), the enhanced scavenging in the high source flux simulations
449 removes more DFe than source fluxes add to the Southern Ocean. Therefore, DFe levels further
450 decrease in the Southern Ocean (Figure 4k, 5e-h) in the high source flux scenarios. The high
451 scavenging in our best model simulation with variable ligands and high source fluxes (#5
452 *Atm+SedFeHigh_LigVar*) reduces DFe, marine productivity and resulting oxygen consumption
453 during remineralization of particulate organic matter, thereby increasing dissolved oxygen
454 concentrations at depth. This effect is significant enough to increase average global dissolved
455 oxygen concentrations by 8% in the model because water masses formed in the Southern Ocean
456 contribute to much of the global deep ocean (Table 3). This emphasizes the importance of
457 simulating a robust global marine iron cycle most importantly in the Southern Ocean.

458 **5 Conclusions**

459 In this study we tested various rates of atmospheric soluble deposition, reductive
460 sedimentary release, and variable ligand distributions within a marine iron component in a global
461 ocean biogeochemical model. The simulations that best reproduce the global DFe observations
462 include highest tested source fluxes and a variable ligand parameterization. The most striking
463 feature in the global DFe observations that supports this hypothesis is the strong gradients that
464 often occur with high concentrations near source fluxes and low concentrations in adjacent open
465 ocean regions. This high source flux/scavenging iron cycling regime causes a relatively short
466 mean residence times of less than a decade in the global oceans and less than a year in the
467 surface ocean. The short residence time implies that the global marine iron cycle is highly
468 sensitive to environmental perturbations in the Anthropocene and geological past. Although
469 uncertainties remain high due to model parameterizations of complex, poorly understood
470 processes and the sparsity of DFe measurements throughout the global ocean, our model-data
471 analysis suggests the marine iron cycle operates with relatively high source fluxes and high
472 scavenging rates.

473 **Acknowledgments, Samples, and Data**

474 This study was funded by the Cluster of Excellence ‘The Future Ocean’. ‘The Future Ocean’ is
475 funded within the framework of the Excellence Initiative by the Deutsche
476 Forschungsgemeinschaft (DFG) on behalf of the German federal and state governments. This
477 project has also received funding from the European Union’s Horizon 2020 research and
478 innovation programme under grant agreement No 820989 (project COMFORT, Our common
479 future ocean in the Earth system – quantifying coupled cycles of carbon, oxygen, and nutrients
480 for determining and achieving safe operating spaces with respect to tipping points). The work
481 reflects only the author’s/authors’ view; the European Commission and their executive agency
482 are not responsible for any use that may be made of the information the work contains. We thank
483 Christoph Völker for helpful comments and suggestions. We acknowledge Choa Luo, Natalie
484 Mahowald and the GESAMP Working Group 38 for making their atmospheric deposition fields
485 available, the GEOTRACES community for making their dissolved iron data available, and the
486 SCOR Working Group 151 Iron Model Intercomparison Project (FeMIP) for support. Model
487 output will be made publicly accessible at GEOMAR open access repository
488 (thredds.geomar.de).

489 **Table 1. Marine Iron Model Configurations**

#	Simulation Name	Atmospheric deposition	Sedimentary release	Ligands	Inorganic Scavenging (kFe_{pp}^a)	Particle Scavenging (kFe_{org}^b)
1	SedFeLow_LigConst	Luo2008 ^c	Elrod2004 ^d	Constant ^e	0.0069	1.2
2	SedFeLow_LigVar	Luo2008	Elrod2004	Variable ^f	0.0052	1.5
3	SedFeMid_LigVar	Luo2008	Dale2015 ^g	Variable	0.0069	2.2
4	SedFeHigh_LigVar	Luo2008	Dale2015 ^h	Variable	0.0081	2.9
5	Atm+SedFeHigh_LigVar	Myrio2018 ⁱ	Dale2015	Variable	0.0098	2.9

490

491 a Inorganic scavenging parameter has units of d^{-1} 492 b Particle scavenging parameter has units of $(gC/m^3)^{-0.58} d^{-1}$

493 c (Luo et al., 2008)

494 d (Elrod et al., 2004)

495 e Constant concentration of 1 nM everywhere in the ocean

496 f Variable ligand parameterization (see section 2.3.3)

497 g Dale et al. (2015) function with reduced maximum flux rate $100 \mu mol m^{-2} d^{-1}$ 498 h Dale et al. (2015) function with suggested maximum flux rate $170 \mu mol m^{-2} d^{-1}$

499 i (Myriokefalitakis et al., 2018)

500 **Table 2. Global Marine Iron Cycle Results**

#	Simulation Name	Atmospheric soluble deposition (Gmol yr ⁻¹)	Reductive Sedimentary release (Gmol yr ⁻¹)	Hydro-thermal (Gmol yr ⁻¹)	Inorganic Scavenging (Gmol yr ⁻¹)	Particle Scavenging (Gmol yr ⁻¹)	Dissolved Iron (nM)	Global Residence time ^a (yr)	Surface Residence time ^b (yr)
1	SedFeLow_LigConst	1.4	15.1	11.4	34.3	22.5	0.68	33.3	3.12
2	SedFeLow_LigVar	1.4	14.6	11.4	30.9	29.3	0.73	35.9	2.56
3	SedFeMid_LigVar	1.4	68.6	11.4	99.3	55.9	0.73	12.2	1.35
4	SedFeHigh_LigVar	1.4	117	11.4	159	83.9	0.73	7.66	0.87
5	Atm+SedFeHigh_LigVar	3.4	114	11.4	162	81.5	0.71	7.49	0.83

501

502 ^aSince our iron model simulates active (re)cycling between particulates and dissolved forms and thus scavenging does not permanently
503 remove bioavailable iron from the system, we calculate residence time based on external fluxes of this global system, i.e. global Fe
504 inventory/ Σ Source Inputs.

505 ^bFor surface residence time, we follow Black et al. (2020) by including the upper 250 meters and account for sinking particulate iron
506 out of this layer as the sink flux. Since our particulate iron pool includes both biogenic (i.e. produced during primary production) and
507 authigenic (i.e. produced by scavenging) iron in the model, this model residence time is comparable to their mean dissolved,
508 biogenic+authigenic estimate, which ranges from 0.1 to 4 years depending on location.

509 **Table 3. Global Marine Biogeochemistry Results**

#	Simulation Name	Net Primary Production (Gt C yr ⁻¹)	Export Production (Gt C yr ⁻¹)	Global O ₂ (mmol m ⁻³)	Southern Ocean O ₂ (mmol m ⁻³)	Suboxic Volume (x10 ¹⁵ m ³)
1	SedFeLow_LigConst	47.0	8.1	167.1	206.3	8.5
2	SedFeLow_LigVar	47.4	7.9	174.6	216.3	7.7
3	SedFeMid_LigVar	47.7	7.9	177.5	220.7	7.7
4	SedFeHigh_LigVar	48.0	7.9	178.6	222.0	7.5
5	Atm+SedFeHigh_LigVar	47.9	7.8	180.5	224.2	6.6

510

511 **Figure 1.** Schematic of the marine iron (Fe) model. See section 2.3 for a full description.

512

513 **Figure 2.** Vertically-integrated, annual fluxes of atmospheric soluble iron deposition (top row)
 514 prescribed on the base (BASE) model simulations from Luo et al. (2008) (a), high scenario
 515 (*Atm+*) from the GESAMP intermodel average (Myriokefalitakis et al., 2018) (b), and their
 516 difference (c). Bottom row: Sedimentary iron release using functions based on Elrod et al.
 517 (2004) (*SedFeLow*) (d) and Dale et al. (2015) (*SedFeHigh*) (e), and their difference (f).

518

519 **Figure 3.** Distribution of variable ligand concentrations in the surface (0-250 meters) ocean (a),
 520 and basin-scale averages in the Atlantic (b), Indian (c), Pacific (d), and Southern (e). Note that
 521 the Southern Ocean sector (>40°S) was excluded from the other basins.

522

523 **Figure 4.** Annually averaged depth profiles of marine iron source inputs (left column), dissolved
 524 iron concentrations (center column), and scavenging rates (right column) in the Global, Atlantic,
 525 Indian-Pacific, and Southern Ocean for model simulations (colored) and dissolved iron
 526 observations (filled black circles). Source inputs (left column) are atmospheric soluble deposition
 527 as large filled symbols in the base (green squares) and high (*Atm+*; red diamonds) scenarios,
 528 sedimentary iron release in the low (*SedFeLow*; blue circles) and high scenarios (*SedFeHigh*;
 529 purple triangles), and hydrothermal flux (open green boxes, applied to all simulations). For
 530 dissolved iron concentrations (center column), lines show model averages in the entire selected
 531 domain, while symbols include model results only where dissolved iron observations exist. Note
 532 that the Southern Ocean sector (>40°S) is excluded from the Atlantic and Indian-Pacific basins.

533

534 **Figure 5.** Annually averaged dissolved iron concentrations in the upper 250 meters in
 535 observations (a), *SedFeLow_LigConst* (b), *SedFeLow_LigVar* (c), *SedFeHigh_LigVar* (e), and
 536 *Atm+SedFeHigh_LigVar* (g). Right column highlights individual effects on dissolved iron
 537 concentrations by showing model differences from variable ligands (i.e.
 538 *SedFeLow_LigVar*–*SedFeLow_LigConst*) (d), high sedimentary iron release (i.e.
 539 *SedFeHigh_LigVar*–*SedFeLow_LigVar*) (f), and high atmospheric soluble deposition (i.e.
 540 *Atm+SedFeHigh_LigVar*–*SedFeHigh_LigVar*) (h).

541

542 **Figure 6.** Comparison of dissolved iron measurements (black circles) in the upper 250 meters
543 with model simulations *SedFeLow_LigConst* (green squares), *SedFeLow_LigVar* (blue circles),
544 *SedFeHigh_LigVar* (purple triangles), *Atm+SedFeHigh_LigVar* (red diamonds) across ocean
545 basin sections in the tropical Pacific (meridional average from 20°S-20°N) (a); central Pacific
546 (zonal averaged from 180°-150°W) (b); Indian (zonal averaged from 20°-100°E) (c); and eastern
547 Atlantic (zonal averaged from 20°W-15°E) (d). Lines show model averages in the entire selected
548 domain, while symbols include model results only at locations where observations exist. Since
549 the core of oxygen deficient zones in the model does not overlap with the real ocean where high
550 dissolved iron concentrations exist in the eastern Pacific (a) and northern Indian (c), we added
551 dissolved iron concentrations directly above the core of the oxygen deficient zones ($O_2 < 5 \text{ mmol}$
552 m^{-3}) in the model as star symbols.

553

554 **Figure 7.** Model-data statistical metrics calculated using all observations (upper panels a-f) and
555 using only GEOTRACES observations (lower panels g-l). Correlation coefficient (left column),
556 standard deviation (center column), root-mean-squared error (right column) are calculated for the
557 global ocean (top rows) and upper 250 meters of the water column (bottom rows). Standard
558 deviation (b,e) and root-mean-squared error (c,f) are normalized by the standard deviation of
559 observations. Note that vertical axes have been adjusted to show the full range in each individual
560 panel.

561 **References**

- 562 Anderson, R. F., Cheng, H., Edwards, R. L., Fleisher, M. Q., Hayes, C. T., Huang, K. F., Kadko,
563 D., Lam, P. J., Landing, W. M., Lao, Y., Lu, Y., Measures, C. I., Moran, S. B., Morton,
564 P. L., Ohnemus, D. C., Robinson, L. F., and Shelley, R. U.: How well can we quantify
565 dust deposition to the ocean?, *Philos Trans A Math Phys Eng Sci*, 374,
566 10.1098/rsta.2015.0285, 2016.
- 567 Aumont, O., Ethé, C., Tagliabue, A., Bopp, L., and Gehlen, M.: PISCES-v2: an ocean
568 biogeochemical model for carbon and ecosystem studies, *Geoscientific Model*
569 *Development*, 8, 2465-2513, 10.5194/gmd-8-2465-2015, 2015.
- 570 Black, E. E., Kienast, S. S., Lemaitre, N., Lam, P. J., Anderson, R. F., Planquette, H., Planchon,
571 F., and Buesseler, K. O.: Ironing Out Fe Residence Time in the Dynamic Upper Ocean,
572 *Global Biogeochemical Cycles*, 34, 10.1029/2020gb006592, 2020.
- 573 Boyd, P. W., and Ellwood, M. J.: The biogeochemical cycle of iron in the ocean, *Nature*
574 *Geoscience*, 3, 675-682, 10.1038/ngeo964, 2010.
- 575 Bruland, K. W., Middag, R., and Lohan, M. C.: 8.2 - Controls of Trace Metals in Seawater, in:
576 *Treatise on Geochemistry (Second Edition)*, edited by: Holland, H. D., and Turekian, K.
577 K., Elsevier, Oxford, 19-51, 2014.
- 578 Bundy, R. M., Boiteau, R. M., McLean, C., Turk-Kubo, K. A., McIlvin, M. R., Saito, M. A., Van
579 Mooy, B. A. S., and Repeta, D. J.: Distinct Siderophores Contribute to Iron Cycling in
580 the Mesopelagic at Station ALOHA, *Frontiers in Marine Science*, 5,
581 10.3389/fmars.2018.00061, 2018.
- 582 Conway, T. M., and John, S. G.: Quantification of dissolved iron sources to the North Atlantic
583 Ocean, *Nature*, 511, 212-215, 10.1038/nature13482, 2014.
- 584 Croot, P. L., Streu, P., and Baker, A. R.: Short residence time for iron in surface seawater
585 impacted by atmospheric dry deposition from Saharan dust events, *Geophysical Research*
586 *Letters*, 31, 10.1029/2004gl020153, 2004.
- 587 Dale, A. W., Nickelsen, L., Scholz, F., Hensen, C., Oschlies, A., and Wallmann, K.: A revised
588 global estimate of dissolved iron fluxes from marine sediments, *Global Biogeochemical*
589 *Cycles*, 29, 691-707, 10.1002/2014gb005017, 2015.
- 590 Eby, M., Zickfeld, K., Montenegro, A., Archer, D., Meissner, K. J., and Weaver, A. J.: Lifetime
591 of Anthropogenic Climate Change: Millennial Time Scales of Potential CO₂ and Surface
592 Temperature Perturbations, *Journal of Climate*, 22, 2501-2511, 10.1175/2008jcli2554.1,
593 2009.
- 594 Elrod, V. A., Berelson, W. M., Coale, K. H., and Johnson, K. S.: The flux of iron from
595 continental shelf sediments: A missing source for global budgets, *Geophysical Research*
596 *Letters*, 31, L12307, 10.1029/2004gl020216, 2004.
- 597 Frants, M., Holzer, M., DeVries, T., and Matear, R.: Constraints on the global marine iron cycle
598 from a simple inverse model, *Journal of Geophysical Research: Biogeosciences*, 121, 28-
599 51, 10.1002/2015jg003111, 2016.
- 600 Galbraith, E. D., Gnanadesikan, A., Dunne, J. P., and Hiscock, M. R.: Regional impacts of iron-
601 light colimitation in a global biogeochemical model, *Biogeosciences*, 7, 1043-1064,
602 10.5194/bg-7-1043-2010, 2010.
- 603 Gent, P. R., and McWilliams, J. C.: Isopycnal Mixing in Ocean Circulation Models, *Journal of*
604 *Physical Oceanography*, 20, 150-155, doi:10.1175/1520-
605 0485(1990)020<0150:IMIOCM>2.0.CO;2, 1990.

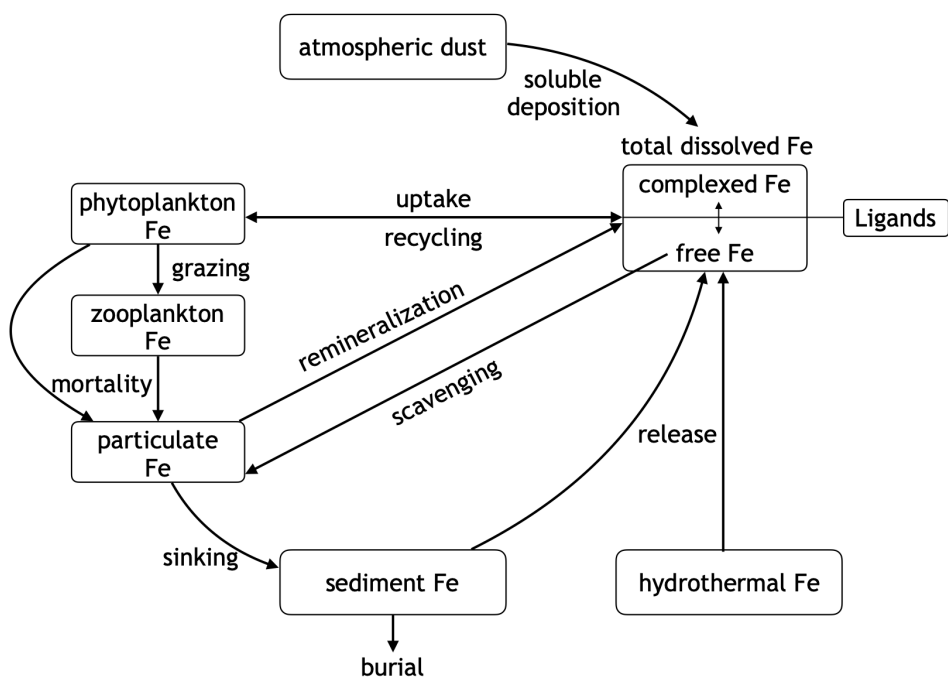
- 606 Getzlaff, J., and Dietze, H.: Effects of increased isopycnal diffusivity mimicking the unresolved
 607 equatorial intermediate current system in an earth system climate model, *Geophysical*
 608 *Research Letters*, 10.1002/grl.50419, 2013.
- 609 Gledhill, M., and Buck, K. N.: The organic complexation of iron in the marine environment: a
 610 review, *Frontiers in microbiology*, 3, 10.3389/fmicb.2012.00069, 2012.
- 611 Homoky, W. B., John, S. G., Conway, T. M., and Mills, R. A.: Distinct iron isotopic signatures
 612 and supply from marine sediment dissolution, *Nat Commun*, 4, 2143,
 613 10.1038/ncomms3143, 2013.
- 614 Honeyman, B. D., Balistrieri, L. S., and Murray, J. W.: Oceanic trace metal scavenging: the
 615 importance of particle concentration, *Deep Sea Research Part A. Oceanographic*
 616 *Research Papers*, 35, 227-246, [https://doi.org/10.1016/0198-0149\(88\)90038-6](https://doi.org/10.1016/0198-0149(88)90038-6), 1988.
- 617 Johnson, K. S., Gordon, R. M., and Coale, K. H.: What controls dissolved iron concentrations in
 618 the world ocean?, *Marine Chemistry*, 57, 137-161, [https://doi.org/10.1016/S0304-](https://doi.org/10.1016/S0304-4203(97)00043-1)
 619 [4203\(97\)00043-1](https://doi.org/10.1016/S0304-4203(97)00043-1), 1997.
- 620 Kalnay, E., Kanamitsu, M., Kistler, R., Collins, W., Deaven, D., Gandin, L., Iredell, M., Saha,
 621 S., White, G., Woollen, J., Zhu, Y., Leetmaa, A., Reynolds, R., Chelliah, M., Ebisuzaki,
 622 W., Higgins, W., Janowiak, J., Mo, K. C., Ropelewski, C., Wang, J., Jenne, R., and
 623 Joseph, D.: The NCEP/NCAR 40-Year Reanalysis Project, *Bulletin of the American*
 624 *Meteorological Society*, 77, 437-471, 10.1175/1520-
 625 0477(1996)077<0437:tnyrp>2.0.co;2, 1996.
- 626 Kvale, K. F., Meissner, K. J., Keller, D. P., Eby, M., and Schmittner, A.: Explicit Planktic
 627 Calcifiers in the University of Victoria Earth System Climate Model, Version 2.9,
 628 *Atmosphere-Ocean*, 53, 332-350, 10.1080/07055900.2015.1049112, 2015.
- 629 Large, W. G., Danabasoglu, G., McWilliams, J. C., Gent, P. R., and Bryan, F. O.: Equatorial
 630 Circulation of a Global Ocean Climate Model with Anisotropic Horizontal Viscosity,
 631 *Journal of Physical Oceanography*, 31, 518-536, doi:10.1175/1520-
 632 0485(2001)031<0518:ECOAGO>2.0.CO;2, 2001.
- 633 Luo, C., Mahowald, N., Bond, T., Chuang, P. Y., Artaxo, P., Siefert, R., Chen, Y., and Schauer,
 634 J.: Combustion iron distribution and deposition, *Global Biogeochemical Cycles*, 22,
 635 GB1012, 10.1029/2007gb002964, 2008.
- 636 Misumi, K., Lindsay, K., Moore, J. K., Doney, S. C., Tsumune, D., and Yoshida, Y.: Humic
 637 substances may control dissolved iron distributions in the global ocean: Implications
 638 from numerical simulations, *Global Biogeochemical Cycles*, 27, 450-462,
 639 10.1002/gbc.20039, 2013.
- 640 Moffett, J. W., Goepfert, T. J., and Naqvi, S. W. A.: Reduced iron associated with secondary
 641 nitrite maxima in the Arabian Sea, *Deep Sea Research Part I: Oceanographic Research*
 642 *Papers*, 54, 1341-1349, 10.1016/j.dsr.2007.04.004, 2007.
- 643 Moore, C. M., Mills, M. M., Arrigo, K. R., Berman-Frank, I., Bopp, L., Boyd, P. W., Galbraith,
 644 E. D., Geider, R. J., Guieu, C., Jaccard, S. L., Jickells, T. D., La Roche, J., Lenton, T. M.,
 645 Mahowald, N. M., Marañón, E., Marinov, I., Moore, J. K., Nakatsuka, T., Oschlies, A.,
 646 Saito, M. A., Thingstad, T. F., Tsuda, A., and Ulloa, O.: Processes and patterns of
 647 oceanic nutrient limitation, *Nature Geoscience*, 6, 701-710, 10.1038/ngeo1765, 2013.
- 648 Moore, J. K., and Braucher, O.: Sedimentary and mineral dust sources of dissolved iron to the
 649 world ocean, *Biogeosciences*, 5, 631-656, 10.5194/bg-5-631-2008, 2008.

- 650 Muglia, J., Somes, C. J., Nickelsen, L., and Schmittner, A.: Combined Effects of Atmospheric
 651 and Seafloor Iron Fluxes to the Glacial Ocean, *Paleoceanography*, 32, 1204-1218,
 652 10.1002/2016pa003077, 2017.
- 653 Myriokefalitakis, S., Ito, A., Kanakidou, M., Nenes, A., Krol, M. C., Mahowald, N. M., Scanza,
 654 R. A., Hamilton, D. S., Johnson, M. S., Meskhidze, N., Kok, J. F., Guieu, C., Baker, A.
 655 R., Jickells, T. D., Sarin, M. M., Bikkina, S., Shelley, R., Bowie, A., Perron, M. M. G.,
 656 and Duce, R. A.: Reviews and syntheses: the GESAMP atmospheric iron deposition
 657 model intercomparison study, *Biogeosciences*, 15, 6659-6684, 10.5194/bg-15-6659-2018,
 658 2018.
- 659 Nickelsen, L., Keller, D. P., and Oeschler, A.: A dynamic marine iron cycle module coupled to
 660 the University of Victoria Earth System Model: the Kiel Marine Biogeochemical Model 2
 661 for UVic 2.9, *Geoscientific Model Development*, 8, 1357-1381, 10.5194/gmd-8-1357-
 662 2015, 2015.
- 663 Parekh, P., Follows, M. J., and Boyle, E.: Modeling the global ocean iron cycle, *Global*
 664 *Biogeochemical Cycles*, 18, n/a-n/a, 10.1029/2003gb002061, 2004.
- 665 Peltier, W. R.: Global glacial isostasy and the surface of the ice-age Earth: The ICE-5G (VM2)
 666 model and GRACE, *Annual Review of Earth and Planetary Sciences*, 32, 111-149,
 667 10.1146/annurev.earth.32.082503.144359, 2004.
- 668 Pham, A. L. D., and Ito, T.: Formation and Maintenance of the GEOTRACES Subsurface-
 669 Dissolved Iron Maxima in an Ocean Biogeochemistry Model, *Global Biogeochemical*
 670 *Cycles*, 32, 932-953, 10.1029/2017gb005852, 2018.
- 671 Pham, A. L. D., and Ito, T.: Ligand Binding Strength Explains the Distribution of Iron in the
 672 North Atlantic Ocean, *Geophysical Research Letters*, 10.1029/2019gl083319, 2019.
- 673 Resing, J. A., Sedwick, P. N., German, C. R., Jenkins, W. J., Moffett, J. W., Sohst, B. M., and
 674 Tagliabue, A.: Basin-scale transport of hydrothermal dissolved metals across the South
 675 Pacific Ocean, *Nature*, 523, 200-203, 10.1038/nature14577, 2015.
- 676 Sarthou, G., Baker, A. R., Blain, S., Achterberg, E. P., Boye, M., Bowie, A. R., Croot, P., Laan,
 677 P., de Baar, H. J. W., Jickells, T. D., and Worsfold, P. J.: Atmospheric iron deposition
 678 and sea-surface dissolved iron concentrations in the eastern Atlantic Ocean, *Deep Sea*
 679 *Research Part I: Oceanographic Research Papers*, 50, 1339-1352,
 680 [https://doi.org/10.1016/S0967-0637\(03\)00126-2](https://doi.org/10.1016/S0967-0637(03)00126-2), 2003.
- 681 Schlitzer, R., Anderson, R. F., Dodas, E. M., Lohan, M., Geibert, W., Tagliabue, A., Bowie, A.,
 682 Jeandel, C., Maldonado, M. T., Landing, W. M., Cockwell, D., Abadie, C., Abouchami,
 683 W., Achterberg, E. P., Agather, A., Aguiar-Islas, A., van Aken, H. M., Andersen, M.,
 684 Archer, C., Auro, M., de Baar, H. J., Baars, O., Baker, A. R., Bakker, K., Basak, C.,
 685 Baskaran, M., Bates, N. R., Bauch, D., van Beek, P., Behrens, M. K., Black, E., Bluhm,
 686 K., Bopp, L., Bouman, H., Bowman, K., Bown, J., Boyd, P., Boye, M., Boyle, E. A.,
 687 Branellec, P., Bridgestock, L., Brissebrat, G., Browning, T., Bruland, K. W., Brumsack,
 688 H.-J., Brzezinski, M., Buck, C. S., Buck, K. N., Buesseler, K., Bull, A., Butler, E., Cai,
 689 P., Mor, P. C., Cardinal, D., Carlson, C., Carrasco, G., Casacuberta, N., Casciotti, K. L.,
 690 Castrillejo, M., Chamizo, E., Chance, R., Charette, M. A., Chaves, J. E., Cheng, H.,
 691 Chever, F., Christl, M., Church, T. M., Closset, I., Colman, A., Conway, T. M., Cossa,
 692 D., Croot, P., Cullen, J. T., Cutter, G. A., Daniels, C., Dehairs, F., Deng, F., Dieu, H. T.,
 693 Duggan, B., Dulaquais, G., Dumousseaud, C., Echevoyen-Sanz, Y., Edwards, R. L.,
 694 Ellwood, M., Fahrbach, E., Fitzsimmons, J. N., Russell Flegal, A., Fleisher, M. Q., van
 695 de Fliedert, T., Frank, M., Friedrich, J., Fripiat, F., Fröllje, H., Galer, S. J. G., Gamo, T.,

- 696 Ganeshram, R. S., Garcia-Orellana, J., Garcia-Solsona, E., Gault-Ringold, M., George,
 697 E., Gerringa, L. J. A., Gilbert, M., Godoy, J. M., Goldstein, S. L., Gonzalez, S. R.,
 698 Grissom, K., Hammerschmidt, C., Hartman, A., Hassler, C. S., Hathorne, E. C., Hatta,
 699 M., Hawco, N., Hayes, C. T., Heimbürger, L.-E., Helgoe, J., Heller, M., Henderson, G.
 700 M., Henderson, P. B., van Heuven, S., Ho, P., Horner, T. J., Hsieh, Y.-T., Huang, K.-F.,
 701 Humphreys, M. P., Isshiki, K., Jacquot, J. E., Janssen, D. J., Jenkins, W. J., John, S.,
 702 Jones, E. M., Jones, J. L., Kadko, D. C., Kayser, R., Kenna, T. C., Khondoker, R., Kim,
 703 T., Kipp, L., Klar, J. K., Klunder, M., Kretschmer, S., Kumamoto, Y., Laan, P., Labatut,
 704 M., Lacan, F., Lam, P. J., Lambelet, M., Lamborg, C. H., Le Moigne, F. A. C., Le Roy,
 705 E., Lechtenfeld, O. J., Lee, J.-M., Lherminier, P., Little, S., López-Lora, M., Lu, Y.,
 706 Masque, P., Mawji, E., McClain, C. R., Measures, C., Mehic, S., Barraqueta, J.-L. M.,
 707 van der Merwe, P., Middag, R., Mieruch, S., Milne, A., Minami, T., Moffett, J. W.,
 708 Moncoiffe, G., Moore, W. S., Morris, P. J., Morton, P. L., Nakaguchi, Y., Nakayama, N.,
 709 Niedermiller, J., Nishioka, J., Nishiuchi, A., Noble, A., Obata, H., Ober, S., Ohnemus, D.
 710 C., van Ooijen, J., O'Sullivan, J., Owens, S., Pahnke, K., Paul, M., Pavia, F., Pena, L. D.,
 711 Peters, B., Planchon, F., Planquette, H., Pradoux, C., Puigcorbé, V., Quay, P., Queroue,
 712 F., Radic, A., Rauschenberg, S., Rehkämper, M., Rember, R., Remenyi, T., Resing, J. A.,
 713 Rickli, J., Rigaud, S., Rijkenberg, M. J. A., Rintoul, S., Robinson, L. F., Roca-Martí, M.,
 714 Rodellas, V., Roeske, T., Rolison, J. M., Rosenberg, M., Roshan, S., Rutgers van der
 715 Loeff, M. M., Ryabenko, E., Saito, M. A., Salt, L. A., Sanial, V., Sarthou, G.,
 716 Schallenberg, C., Schauer, U., Scher, H., Schlosser, C., Schnetger, B., Scott, P., Sedwick,
 717 P. N., Semiletov, I., Shelley, R., Sherrell, R. M., Shiller, A. M., Sigman, D. M., Singh, S.
 718 K., Slagter, H. A., Slater, E., Smethie, W. M., Snaith, H., Sohrin, Y., Sohst, B., Sonke, J.
 719 E., Speich, S., Steinfeldt, R., Stewart, G., Stichel, T., Stirling, C. H., Stutsman, J., Swarr,
 720 G. J., Swift, J. H., Thomas, A., Thorne, K., Till, C. P., Till, R., Townsend, A. T.,
 721 Townsend, E., Tuerena, R., Twining, B. S., Vance, D., Velazquez, S., Venchiarutti, C.,
 722 Villa-Alfageme, M., Vivancos, S. M., Voelker, A. H. L., Wake, B., Warner, M. J.,
 723 Watson, R., van Weerlee, E., Alexandra Weigand, M., Weinstein, Y., Weiss, D.,
 724 Wisotzki, A., Woodward, E. M. S., Wu, J., Wu, Y., Wuttig, K., Wyatt, N., Xiang, Y.,
 725 Xie, R. C., Xue, Z., Yoshikawa, H., Zhang, J., Zhang, P., Zhao, Y., Zheng, L., Zheng, X.-
 726 Y., Zieringer, M., Zimmer, L. A., Ziveri, P., Zunino, P., and Zurbriick, C.: The
 727 GEOTRACES Intermediate Data Product 2017, *Chemical Geology*, 493, 210-223,
 728 <https://doi.org/10.1016/j.chemgeo.2018.05.040>, 2018.
- 729 Schmittner, A., and Egbert, G. D.: An improved parameterization of tidal mixing for ocean
 730 models, *Geoscientific Model Development*, 7, 211-224, 10.5194/gmd-7-211-2014, 2014.
- 731 Schmittner, A., and Somes, C. J.: Complementary constraints from carbon (¹³C) and nitrogen
 732 (¹⁵N) isotopes on the glacial ocean's soft-tissue biological pump, *Paleoceanography*, 31,
 733 669-693, 10.1002/2015PA002905, 2016.
- 734 Somes, C., Schmittner, A., Muglia, J., and Oschlies, A.: A three-dimensional model of the
 735 marine nitrogen cycle during the Last Glacial Maximum constrained by sedimentary
 736 isotopes, *Frontiers in Marine Science*, 4, 10.3389/fmars.2017.00108, 2017.
- 737 Somes, C. J., Schmittner, A., Galbraith, E. D., Lehmann, M. F., Altabet, M. A., Montoya, J. P.,
 738 Letelier, R. M., Mix, A. C., Bourbonnais, A., and Eby, M.: Simulating the global
 739 distribution of nitrogen isotopes in the ocean, *Global Biogeochem. Cycles*, 24, GB4019,
 740 10.1029/2009gb003767, 2010.

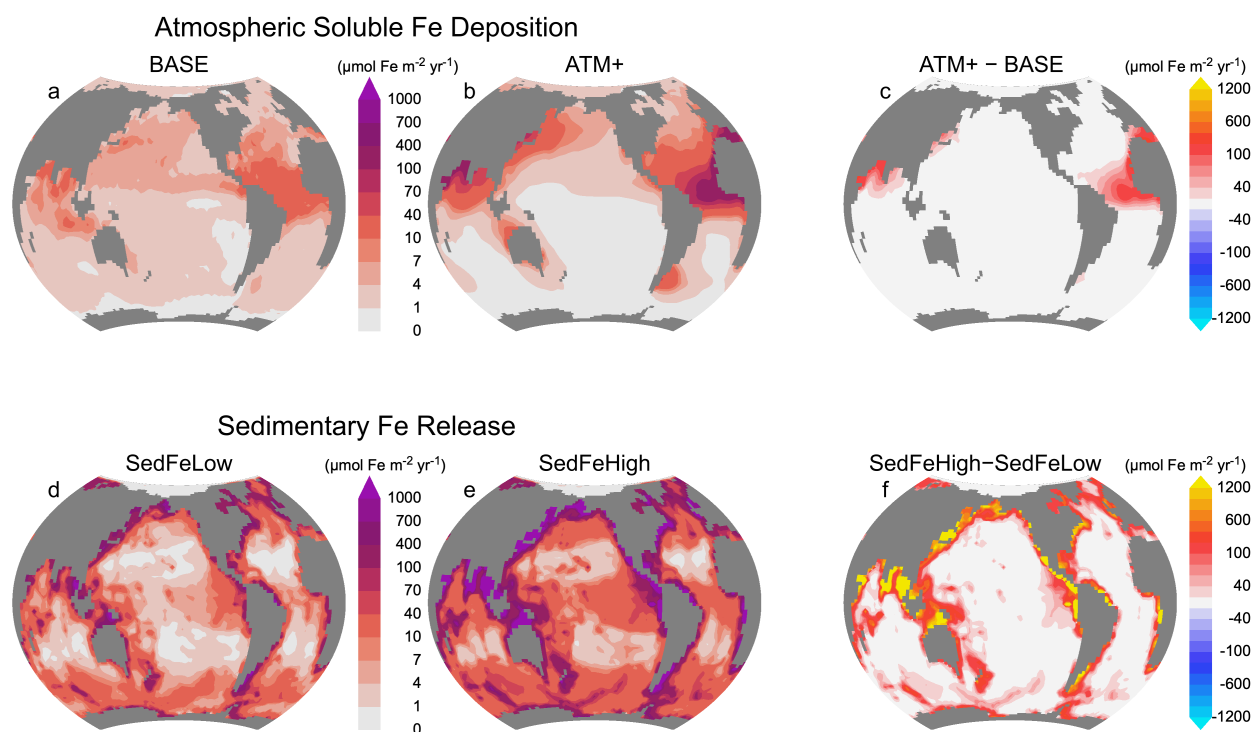
- 741 Somes, C. J., and Oschlies, A.: On the influence of “non-Redfield” dissolved organic nutrient
 742 dynamics on the spatial distribution of N₂ fixation and the size of the marine fixed
 743 nitrogen inventory, *Global Biogeochemical Cycles*, 29, 973-993,
 744 10.1002/2014GB005050, 2015.
- 745 Tagliabue, A., Bopp, L., Dutay, J.-C., Bowie, A. R., Chever, F., Jean-Baptiste, P., Bucciarelli, E.,
 746 Lannuzel, D., Remenyi, T., Sarthou, G., Aumont, O., Gehlen, M., and Jeandel, C.:
 747 Hydrothermal contribution to the oceanic dissolved iron inventory, *Nature Geoscience*, 3,
 748 252-256, 10.1038/ngeo818, 2010.
- 749 Tagliabue, A., and Völker, C.: Towards accounting for dissolved iron speciation in global ocean
 750 models, *Biogeosciences*, 8, 3025-3039, 10.5194/bg-8-3025-2011, 2011.
- 751 Tagliabue, A., Mtshali, T., Aumont, O., Bowie, A. R., Klunder, M. B., Roychoudhury, A. N.,
 752 and Swart, S.: A global compilation of dissolved iron measurements: focus on
 753 distributions and processes in the Southern Ocean, *Biogeosciences*, 9, 2333-2349,
 754 10.5194/bg-9-2333-2012, 2012.
- 755 Tagliabue, A., Aumont, O., DeAth, R., Dunne, J. P., Dutkiewicz, S., Galbraith, E., Misumi, K.,
 756 Moore, J. K., Ridgwell, A., Sherman, E., Stock, C., Vichi, M., Völker, C., and Yool, A.:
 757 How well do global ocean biogeochemistry models simulate dissolved iron
 758 distributions?, *Global Biogeochemical Cycles*, 30, 149-174, 10.1002/2015gb005289,
 759 2016.
- 760 Tagliabue, A., Bowie, A. R., Boyd, P. W., Buck, K. N., Johnson, K. S., and Saito, M. A.: The
 761 integral role of iron in ocean biogeochemistry, *Nature*, 543, 51-59, 10.1038/nature21058,
 762 2017.
- 763 Völker, C., and Tagliabue, A.: Modeling organic iron-binding ligands in a three-dimensional
 764 biogeochemical ocean model, *Marine Chemistry*, 173, 67-77,
 765 10.1016/j.marchem.2014.11.008, 2015.
- 766 Weaver, A. J., Eby, M., Wiebe, E. C., Bitz, C. M., Duffy, P. B., Ewen, T. L., Fanning, A. F.,
 767 Holland, M. M., MacFadyen, A., Matthews, H. D., Meissner, K. J., Saenko, O.,
 768 Schmittner, A., Wang, H., and Yoshimori, M.: The UVic earth system climate model:
 769 Model description, climatology, and applications to past, present and future climates,
 770 *Atmosphere-Ocean*, 39, 361 - 428, 2001.
- 771 Yao, W., Kvale, K. F., Achterberg, E., Koeve, W., and Oschlies, A.: Hierarchy of calibrated
 772 global models reveals improved distributions and fluxes of biogeochemical tracers in
 773 models with explicit representation of iron, *Environmental Research Letters*, 14, 114009,
 774 10.1088/1748-9326/ab4c52, 2019.
- 775 Ye, Y., and Völker, C.: On the Role of Dust-Deposited Lithogenic Particles for Iron Cycling in
 776 the Tropical and Subtropical Atlantic, *Global Biogeochemical Cycles*, 31, 1543-1558,
 777 10.1002/2017gb005663, 2017.
- 778
- 779

780 Figure 1



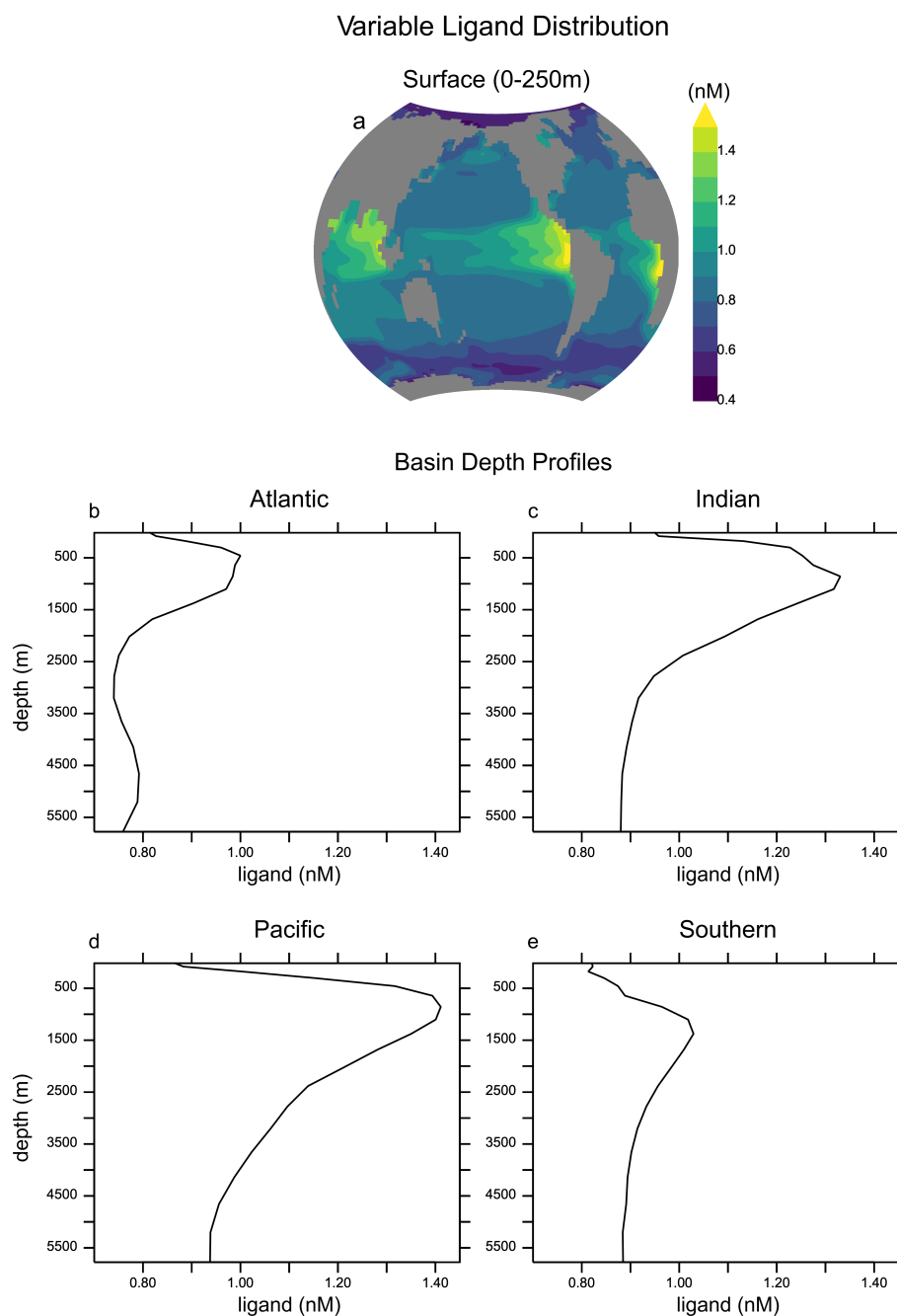
781 **Figure 1.** Schematic of the marine iron (Fe) model. See section 2.3 for a full description.

782 Figure 2



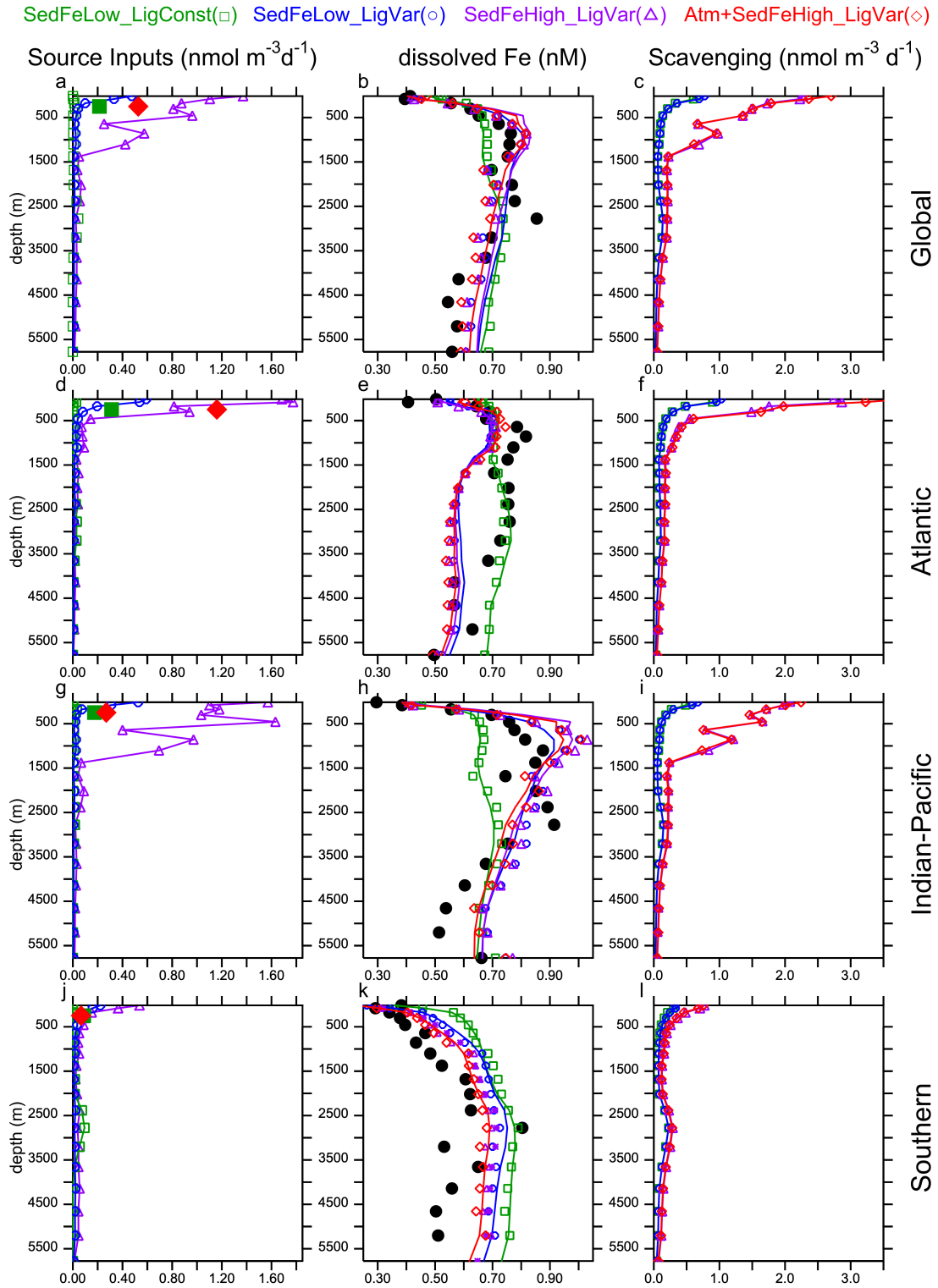
783 **Figure 2.** Vertically-integrated, annual fluxes of atmospheric soluble iron deposition (top row)
 784 prescribed on the base (BASE) model simulations from Luo et al. (2008) (a), high scenario
 785 (*Atm+*) from the GESAMP intermodel average (Myriokefalitakis et al., 2018) (b), and their
 786 difference (c). Bottom row: Sedimentary iron release using functions based on Elrod et al.
 787 (2004) (*SedFeLow*) (d) and Dale et al. (2015) (*SedFeHigh*) (e), and their difference (f).

788 Figure 3



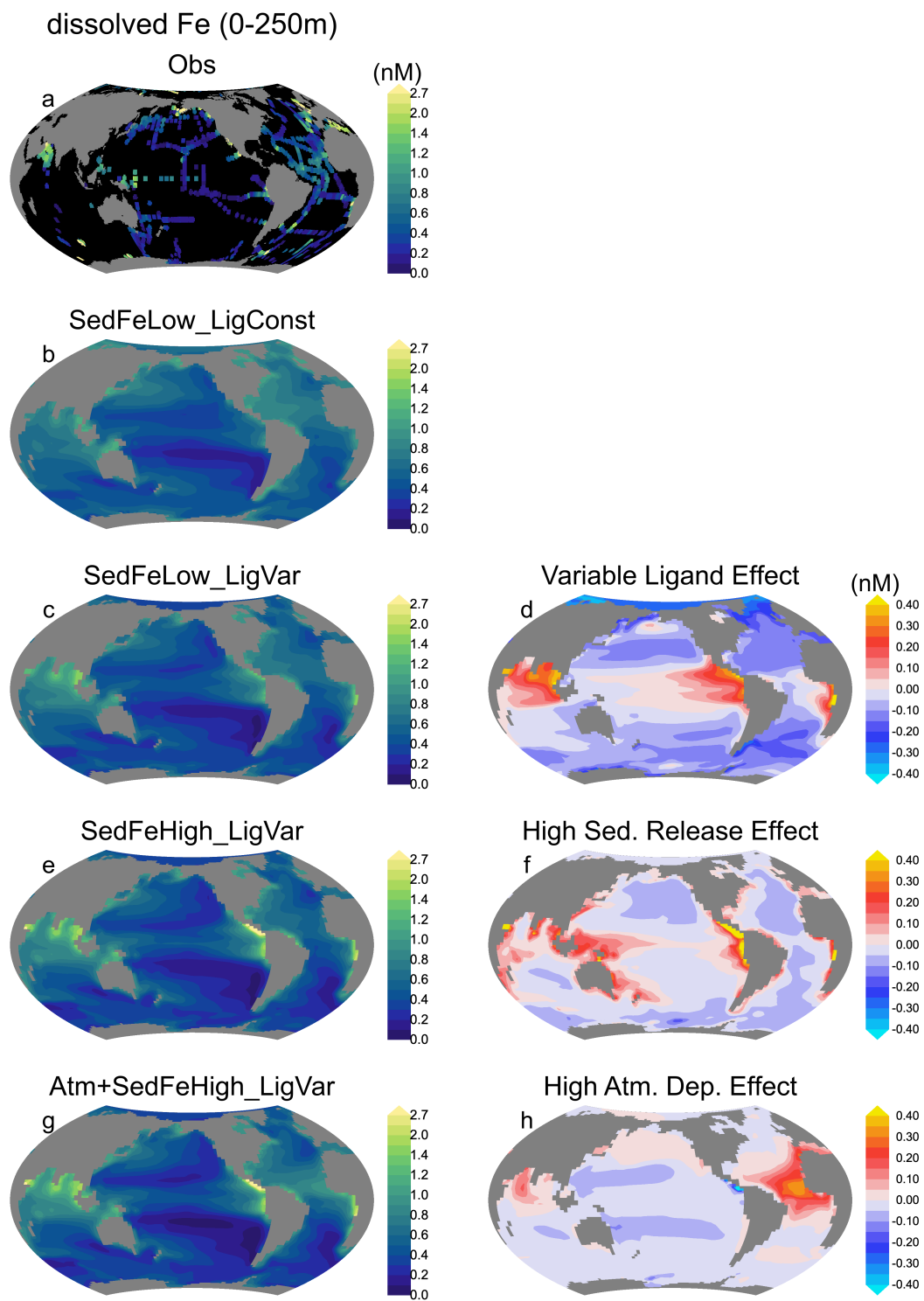
789 **Figure 3.** Distribution of variable ligand concentrations in the surface (0-250 meters) ocean (a),
 790 and basin-scale averages in the Atlantic (b), Indian (c), Pacific (d), and Southern (e). Note that
 791 the Southern Ocean sector ($>40^{\circ}\text{S}$) was excluded from the other basins.
 792

793 Figure 4



794 **Figure 4.** Annually averaged depth profiles of marine iron source inputs (left column), dissolved
795 iron concentrations (center column), and scavenging rates (right column) in the Global, Atlantic,
796 Indian-Pacific, and Southern Ocean for model simulations (colored) and dissolved iron
797 observations (filled black circles). Source inputs (left column) are atmospheric soluble deposition
798 as large filled symbols in the base (green squares) and high (Atm+; red diamonds) scenarios,
799 sedimentary iron release in the low (*SedFeLow*; blue circles) and high scenarios (*SedFeHigh*;
800 purple triangles), and hydrothermal flux (open green boxes, applied to all simulations). For
801 dissolved iron concentrations (center column), lines show model averages in the entire selected
802 domain, while symbols include model results only where dissolved iron observations exist. Note
803 that the Southern Ocean sector (>40°S) is excluded from the Atlantic and Indian-Pacific basins.

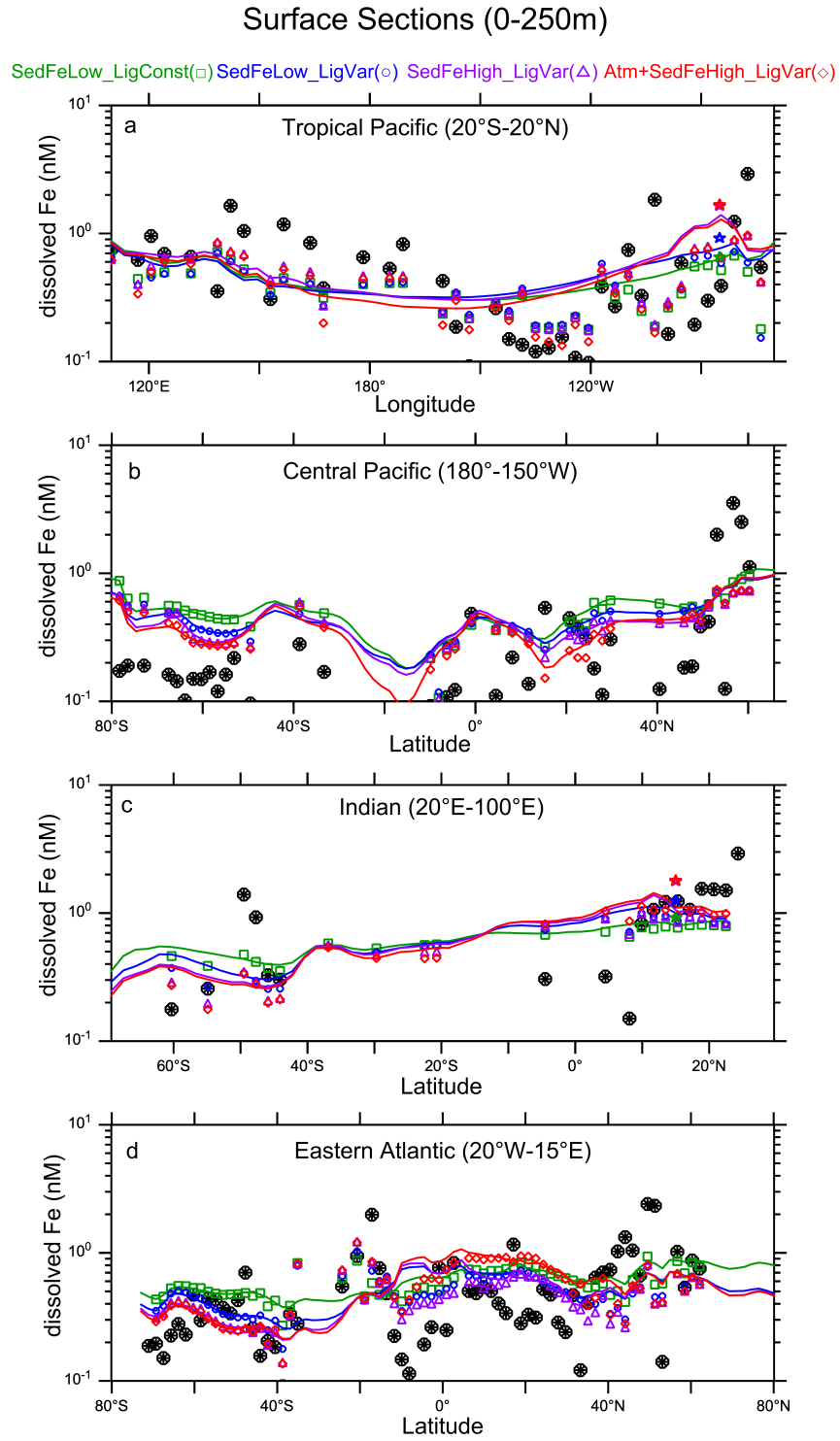
804 Figure 5.



805

806 **Figure 5.** Annually averaged dissolved iron concentrations in the upper 250 meters in
807 observations (a), *SedFeLow_LigConst* (b), *SedFeLow_LigVar* (c), *SedFeHigh_LigVar* (e), and
808 *Atm+SedFeHigh_LigVar* (g). Right column highlights individual effects on dissolved iron
809 concentrations by showing model differences from variable ligands (i.e.
810 *SedFeLow_LigVar*–*SedFeLow_LigConst*) (d), high sedimentary iron release (i.e.
811 *SedFeHigh_LigVar*–*SedFeLow_LigVar*) (f), and high atmospheric soluble deposition (i.e.
812 *Atm+SedFeHigh_LigVar*–*SedFeHigh_LigVar*) (h).

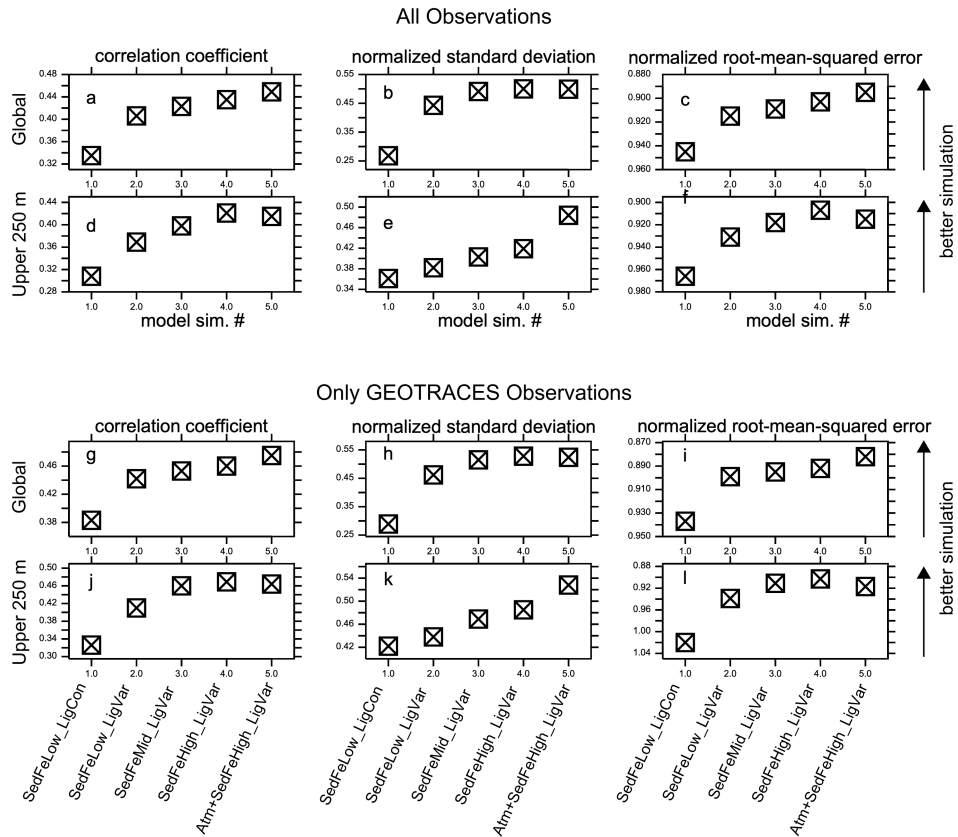
813 Figure 6



814

815 **Figure 6.** Comparison of dissolved iron measurements (black circles) in the upper 250 meters
816 with model simulations *SedFeLow_LigConst* (green squares), *SedFeLow_LigVar* (blue circles),
817 *SedFeHigh_LigVar* (purple triangles), *Atm+SedFeHigh_LigVar* (red diamonds) across ocean
818 basin sections in the tropical Pacific (meridional average from 20°S-20°N) (a); central Pacific
819 (zonal averaged from 180°-150°W) (b); Indian (zonal averaged from 20°-100°E) (c); and eastern
820 Atlantic (zonal averaged from 20°W-15°E) (d). Lines show model averages in the entire selected
821 domain, while symbols include model results only at locations where observations exist. Since
822 the core of oxygen deficient zones in the model does not overlap with the real ocean where high
823 dissolved iron concentrations exist in the eastern Pacific (a) and northern Indian (c), we added
824 dissolved iron concentrations directly above the core of the oxygen deficient zones ($O_2 < 5 \text{ mmol}$
825 m^{-3}) in the model as star symbols.

826 Figure 7



827

828 **Figure 7.** Model-data statistical metrics calculated using all observations (upper panels a-f) and
 829 using only GEOTRACES observations (lower panels g-l). Correlation coefficient (left column),
 830 standard deviation (center column), root-mean-squared error (right column) are calculated for the
 831 global ocean (top rows) and upper 250 meters of the water column (bottom rows). Standard
 832 deviation (b,e) and root-mean-squared error (c,f) are normalized by the standard deviation of
 833 observations. Note that vertical axes have been adjusted to show the full range in each individual
 834 panel.

1

Submitted to

2

Global Biogeochemical Cycles

3

Supporting Information for

4

Constraining global marine iron source and scavenging fluxes with GEOTRACES

5

dissolved iron measurements in an ocean biogeochemical model

6

Christopher J. Somes¹, Andrew W. Dale¹, Klaus Wallmann¹, Florian Scholz¹,

7

Wanxuan Yao¹, Andreas Oschlies¹, Juan Muglia², Andreas Schmittner³, Eric P.

8

Achterberg¹

9

¹ GEOMAR Helmholtz Centre for Ocean Research Kiel, 24105 Kiel, Germany

10

² Centro para el Estudio de los Sistemas Marinos, CONICET, 2915 Boulevard Brown,

11

U9120ACD, Puerto Madryn, Argentina

12

³ College of Earth, Ocean, and Atmospheric Sciences, Oregon State University, Corvallis,

13

Oregon 97331, USA

14

Corresponding author: Christopher J. Somes (csomes@geomar.de)

15

Contents of this file

16

Text S1 to S2

17

Table S1

18

Figures S1 to S3

19

Introduction

20

This section documents minor changes made from previously published versions

21

(Somes et al., 2017;Muglia et al., 2017) that were applied to all model simulations in this

22

study. The core model code is based on the Model of Ocean Biogeochemistry and

23

Isotopes (MOBI), version 2.0 (<https://github.com/OSU-CEOAS-Schmittner/UVic2.9>),

24

which is based on the University of Victoria (UVic) Earth System Model of intermediate

25

complexity (Eby et al., 2013;Weaver et al., 2001).

26 **Text S1. Physical Model**

27 We applied the background vertical mixing setup from Somes et al. (2017) to the
28 default MOBI 2.0 version. This setup applies background vertical mixing of $0.15 \text{ cm}^2 \text{ s}^{-1}$
29 in the ocean interior consistent with open ocean microstructure observations (Fischer et
30 al., 2013), which caused a reduction in the large-scale overturning and an
31 underestimation of $\Delta^{14}\text{C}$ values. In order to reinvigorate the large-scale circulation,
32 we increased the tidal mixing efficiency parameter to 0.28 (from 0.2), applied a
33 background horizontal diffusivity of $20 \text{ m}^2 \text{ s}^{-1}$, and increased the atmospheric moisture
34 diffusivity in the Southern Ocean by 20% (e.g. Muglia & Schmittner (2015)), all of
35 which contributed to an improved representation of $\Delta^{14}\text{C}$ (Figure S1).

36 **Text S2. Marine Biogeochemical Model**

37 Since MOBI version 2.0 integrated the latest improvements to the nitrogen
38 (Somes and Oschlies, 2015), carbon chemistry (Kvale et al., 2015), and iron (Muglia et
39 al., 2017), minor parameter changes were made to achieve a best fit to nutrient
40 distribution (Figure S1, Table S1). Other structural changes are documented below.

41 The production of semi-refractory dissolved organic matter (DOM) has been
42 modified to now include an additional source term from the remineralization of
43 particulate organic matter (POM), along with phytoplankton mortality that previous
44 versions Somes & Oschlies (2015) used. This new term represents DOM production by
45 heterotrophic bacteria as they respire POM. The two DOM production factors have
46 similar spatial patterns, but with the bacterial term based on POM remineralization
47 extending to greater depths. The production fraction parameters (see Table S1) were
48 chosen so they represent roughly equivalent total DOM production rate when integrated
49 over the global ocean, and that they produce surface DON concentrations that are
50 consistent with observations (Figure S2).

51 We have modified the low oxygen threshold including the reduction of dissolved
52 iron (DFe) scavenging in the model. This parameterization was implemented to account
53 for elevated DFe concentrations that exist in low oxygen waters associated with redox
54 cycling including high nitrite concentrations, although it remains unclear exactly what

55 processes contribute to these elevated low oxygen DFe concentrations (Moffett et al.,
56 2015). Previous model versions applied a sharp threshold gradient at the dissolved O₂
57 concentration 5 mmol m⁻³ (Figure S3). However, elevated DFe only exists in lower
58 dissolved O₂ concentrations <~2 mmol m⁻³, so in this study we apply a function that has a
59 sharper gradient at lower dissolved O₂ concentrations (red line in Figure S3) using the
60 equation $\tanh(\kappa \cdot O_2)$ where $\kappa=0.25$.

61 Sedimentary carbon oxidation (C_{ox}) has been modified in all simulations
62 following the Niemeyer et al. (2017) implementation of Flögel et al. (2011). This scheme
63 estimates carbon oxidation from the difference between sinking particulate flux entering
64 the sediment and burial. It has been constructed using a global compilation of
65 sedimentary data that shows higher carbon burial efficiency, and thus lower carbon
66 oxidation in continental margins (Burial=0.14·RR_{POC}^{1.11}) compared to the deep-sea
67 (Burial=0.014·RR_{POC}^{1.05}) sediments. Instead of applying an abrupt transition at 1000
68 meters depth as in Niemeyer et al. (2017) between these surface and deep sea systems,
69 we applied a linear transition to the numerator and exponent coefficients from 500 meters
70 to 1500 meters. Note that previous model marine iron versions (e.g. Nickelsen et al.
71 (2015); Muglia et al. (2017)) applied the temperature-dependent water column
72 remineralization rate to organic matter sinking into sediments to estimate carbon
73 oxidation in the sediments which does not capture the sedimentary carbon dynamics
74 shown in Flögel et al. (2011).

Table S1. Marine Ecosystem-Biogeochemistry Parameters

<i>Parameter</i>	<i>Symbol</i>	<i>Value</i>	<i>Units</i>
<i>Phytoplankton</i>			
Initial slope of P-I curve	α	0.1	$(W\ m^{-2})^{-1}\ d^{-1}$
Photosynthetically active radiation	PAR	0.43	-
Light attenuation in water	k_w	0.04	m^{-1}
Light attenuation through phytoplankton	k_c	0.03	$m^{-1}(mmol\ m^{-3})^{-1}$
Light attenuation through sea ice	k_i	5	m^{-1}
NO ₃ uptake half-saturation	k_{NO3}	0.7	$mmol\ m^{-3}$
PO ₄ uptake half-saturation	k_{PO4}	0.044	$mmol\ m^{-3}$
DOP assimilation handicap	h_{DOP}	0.5	
minimum Fe uptake half-saturation	k_{Femin}	0.05	$nmol\ m^{-3}$
maximum Fe uptake half-saturation	k_{Femax}	0.5	$nmol\ m^{-3}$
Maximum growth rate (at 0°C)	a_0	0.6	d^{-1}
Phytoplankton fast-recycling rate (at 0°C)	μ_{PO0}	0.001	d^{-1}
Phytoplankton specific mortality rate	v_{PO}	0.03	d^{-1}
<i>Calcifying Phytoplankton (P_C)</i>			
Maximum growth rate (at 0°C)	a_0	0.3	d^{-1}
CaCO ₃ :POC production ratio	$R_{CaCO3:POC}$	0.065	0.065
NO ₃ uptake half-saturation	k_{NO3}	0.35	$mmol\ m^{-3}$
PO ₄ uptake half-saturation	k_{PO4}	0.022	$mmol\ m^{-3}$
minimum Fe uptake half-saturation	k_{Femin}	0.025	$nmol\ m^{-3}$
maximum Fe uptake half-saturation	k_{Femax}	0.25	$nmol\ m^{-3}$
<i>Diazotrophic Phytoplankton (P_D)</i>			

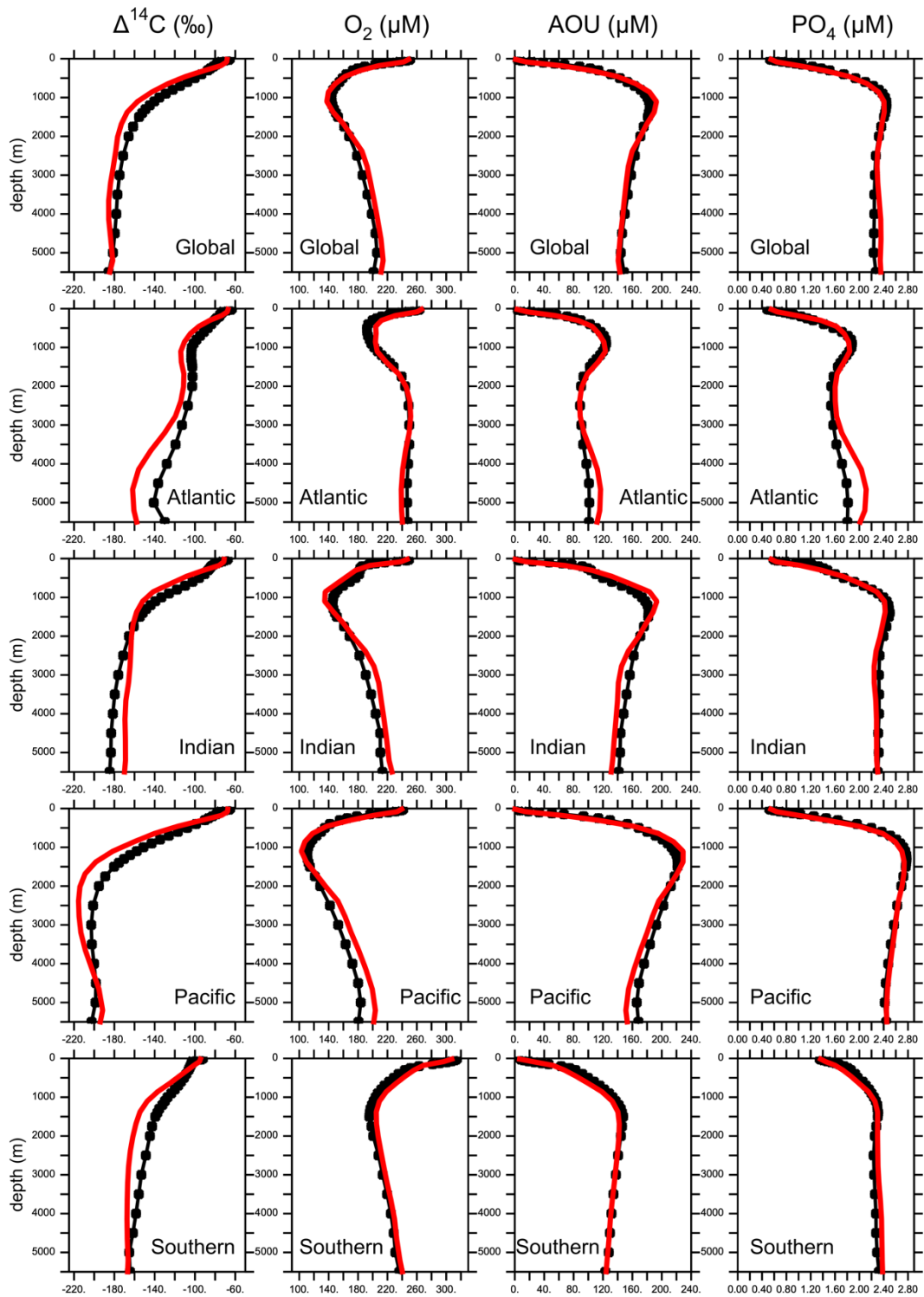
<i>Parameter</i>	<i>Symbol</i>	<i>Value</i>	<i>Units</i>
Diazotroph growth handicap	h_{PD}	0.07	-
Fe uptake half-saturation	k_{Fe}	0.16	nmol m^{-3}
Diazotroph fast-recycling rate (at 0°C)	μ_{PD0}	0.004	d^{-1}
Diazotroph specialist grazing rate	ν_{PD}	0.7	d^{-1}
Diazotroph NO_3 uptake threshold	U_{NO_3}	5	mmol m^{-3}
<i>Zooplankton (Z)</i>			
Assimilation efficiency	γ	0.7	
Maximum grazing rate (at 0°C)	g_Z	0.5	d^{-1}
Growth efficiency	ϖ	0.6	
Mortality	m_z	0.02	d^{-1}
Grazing preference P_O	Ψ_{P_O}	0.26	
Grazing preference P_D	Ψ_{P_D}	0.04	
Grazing preference P_C	Ψ_{P_C}	0.26	
Grazing preference Z	Ψ_Z	0.18	
Grazing preference D	Ψ_D	0.26	
Grazing half-saturation	k_{graz}	0.15	mmol N m^{-3}
<i>Detritus (D)</i>			
Remineralization rate	μ_{D0}	0.07	d^{-1}
Sinking speed at surface	w_{D0}	20	m d^{-1}
Increase of sinking speed with depth	m_w	0.05	d^{-1}

<i>Parameter</i>	<i>Symbol</i>	<i>Value</i>	<i>Units</i>
E-folding temperature of biological rates	T_b	15.65	°C
<i>Dissovled Organic Matter</i>			
phytoplankton DOM production factor	σ_{PDOM}	0.08	
bacterial DOM production factor	σ_{DDOM}	0.02	
DON remineralization rate (at 0°C)	λ_{DON0}	9.4E-6	d ⁻¹
DOP remineralization rate (at 0°C)	λ_{DOP0}	1.9E-5	d ⁻¹
<i>Elemental Ratios</i>			
Molar Oxygen:Nitrogen	$R_{\text{O:N}}$	11	
Molar Carbon:Nitrogen	$R_{\text{C:N}}$	7	
Molar Iron:Nitrogen	$R_{\text{Fe:N}}$	38.5	μmol Fe / mol N
Phytoplankton Nitrogen:Phosphorus	$R_{\text{N:P}_{\text{PO}}}$	16	
Diazotroph Nitrogen:Phosphorus	$R_{\text{N:P}_{\text{PD}}}$	28	
Detritus Nitrogen:Phosphorus	$R_{\text{N:PD}}$	16	
Zooplankton Nitrogen:Phosphorus	$R_{\text{N:PZ}}$	16	

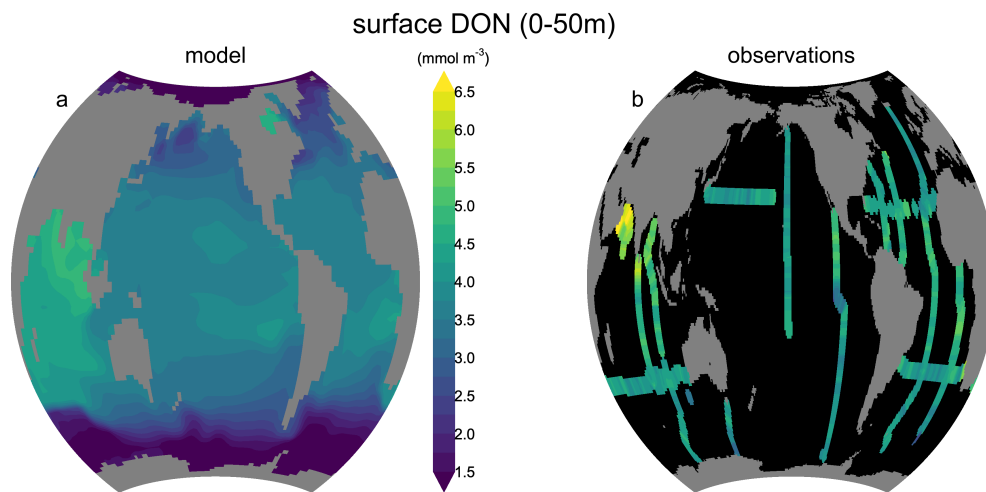
76

77

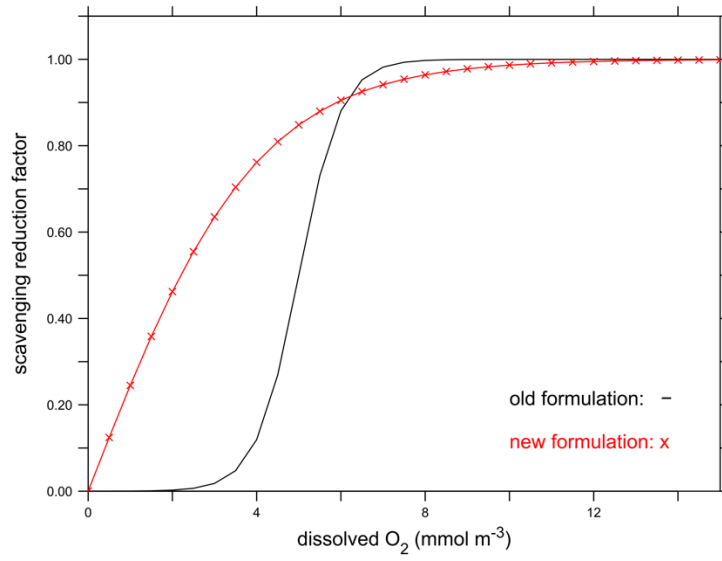
78



80 **Figure S1.** Model-data comparison of basin scale average of radiocarbon ($\Delta^{14}\text{C}$) with
81 GLODAP observations (Key et al., 2004) (left column), and dissolved oxygen (O_2),
82 apparent oxygen utilization (AOU, center column), and phosphate (PO_4 , right column)
83 with World Ocean Atlas observations (Garcia et al., 2010a; Garcia et al., 2010b) (black
84 circles) and the model simulation #5 *Atm+SedFeHigh_LigVar* (red lines).



85
86 **Figure S2.** Surface (0-50 meters) dissolved organic nitrogen (DON) concentrations in the
87 model simulation #5 *Atm+SedFeHigh_LigVar* and observations (Somes and Oschlies,
88 2015; Letscher et al., 2013). Note that the model only includes semi-refractory DON,
89 whereas the observations include total DON.



90
91

Figure S3. Modified function that reduces scavenging in oxygen deficient zones.

92 **References**

- 93
- 94 Eby, M., Weaver, A. J., Alexander, K., Zickfeld, K., Abe-Ouchi, A., Cimatoribus, A. A.,
95 Crespin, E., Drijfhout, S. S., Edwards, N. R., Eliseev, A. V., Feulner, G., Fichefet, T.,
96 Forest, C. E., Goosse, H., Holden, P. B., Joos, F., Kawamiya, M., Kicklighter, D.,
97 Kienert, H., Matsumoto, K., Mokhov, I. I., Monier, E., Olsen, S. M., Pedersen, J. O.
98 P., Perrette, M., Philippon-Berthier, G., Ridgwell, A., Schlosser, A., Schneider von
99 Deimling, T., Shaffer, G., Smith, R. S., Spahni, R., Sokolov, A. P., Steinacher, M.,
100 Tachiiri, K., Tokos, K., Yoshimori, M., Zeng, N., and Zhao, F.: Historical and
101 idealized climate model experiments: an intercomparison of Earth system models of
102 intermediate complexity, *Clim. Past*, 9, 1111-1140, 10.5194/cp-9-1111-2013, 2013.
- 103 Fischer, T., Banyte, D., Brandt, P., Dengler, M., Krahnemann, G., Tanhua, T., and Visbeck,
104 M.: Diapycnal oxygen supply to the tropical North Atlantic oxygen minimum zone,
105 *Biogeosciences*, 10, 5079-5093, 10.5194/bg-10-5079-2013, 2013.
- 106 Flögel, S., Wallmann, K., Poulsen, C. J., Zhou, J., Oschlies, A., Voigt, S., and Kuhnt, W.:
107 Simulating the biogeochemical effects of volcanic CO₂ degassing on the oxygen-state
108 of the deep ocean during the Cenomanian/Turonian Anoxic Event (OAE2), *Earth and
109 Planetary Science Letters*, 305, 371-384, 10.1016/j.epsl.2011.03.018, 2011.
- 110 Garcia, H. E., Locarnini, R. A., Boyer, T. P., Antonov, J. I., Baranov, O. K., Zweng, M.
111 M., and Johnson, D. R.: World Ocean Atlas 2009, Volume 3: Dissolved Oxygen,
112 Apparent Oxygen Utilization, and Oxygen Saturation, in: NOAA Atlas NESDIS 70,
113 edited by: Levitus, S., U.S. Government Printing Office, Washington, D.C., 344,
114 2010a.
- 115 Garcia, H. E., Locarnini, R. A., Boyer, T. P., Antonov, J. I., Zweng, M. M., Baranov, O.
116 K., and Johnson, D. R.: World Ocean Atlas 2009, Volume 4: Nutrients (phosphate,
117 nitrate, silicate), in: NOAA Atlas NESDIS 71, edited by: Levitus, S., U.S.
118 Government Printing Office, Washington, D. C., 398, 2010b.
- 119 Key, R. M., Kozyr, A., Sabine, C. L., Lee, K., Wanninkhof, R., Bullister, J. L., Feely, R.
120 A., Millero, F. J., Mordy, C., and Peng, T. H.: A global ocean carbon climatology:
121 Results from Global Data Analysis Project (GLODAP), *Global Biogeochemical
122 Cycles*, 18, GB4031, 10.1029/2004gb002247, 2004.
- 123 Kvale, K. F., Meissner, K. J., Keller, D. P., Eby, M., and Schmittner, A.: Explicit Planktic
124 Calcifiers in the University of Victoria Earth System Climate Model, Version 2.9,
125 *Atmosphere-Ocean*, 53, 332-350, 10.1080/07055900.2015.1049112, 2015.
- 126 Letscher, R. T., Hansell, D. A., Carlson, C. A., Lumpkin, R., and Knapp, A. N.:
127 Dissolved organic nitrogen in the global surface ocean: Distribution and fate, *Global
128 Biogeochemical Cycles*, n/a-n/a, 10.1029/2012GB004449, 2013.
- 129 Moffett, J. W., Vedamati, J., Goepfert, T. J., Pratihary, A., Gauns, M., and Naqvi, S. W.
130 A.: Biogeochemistry of iron in the Arabian Sea, *Limnology and Oceanography*, 60,
131 1671-1688, 10.1002/lno.10132, 2015.
- 132 Muglia, J., and Schmittner, A.: Wind stress increases glacial atlantic overturning in
133 climate models, *Geophysical Research Letters*, 42, 9862-9868,
134 10.1002/2015gl064583, 2015.
- 135 Muglia, J., Somes, C. J., Nickelsen, L., and Schmittner, A.: Combined Effects of
136 Atmospheric and Seafloor Iron Fluxes to the Glacial Ocean, *Paleoceanography*, 32,
137 1204-1218, 10.1002/2016pa003077, 2017.

138 Nickelsen, L., Keller, D. P., and Oeschler, A.: A dynamic marine iron cycle module
139 coupled to the University of Victoria Earth System Model: the Kiel Marine
140 Biogeochemical Model 2 for UVic 2.9, *Geoscientific Model Development*, 8, 1357-
141 1381, 10.5194/gmd-8-1357-2015, 2015.

142 Niemeier, D., Kemena, T. P., Meissner, K. J., and Oeschler, A.: A model study of
143 warming-induced phosphorus-oxygen feedbacks in open-ocean oxygen minimum
144 zones on millennial timescales, *Earth Syst. Dynam.*, 2017, 2, 357-367, 10.5194/esd-8-
145 357-2017, 2017.

146 Somes, C., Schmittner, A., Muglia, J., and Oeschler, A.: A three-dimensional model of
147 the marine nitrogen cycle during the Last Glacial Maximum constrained by
148 sedimentary isotopes, *Frontiers in Marine Science*, 4, 10.3389/fmars.2017.00108,
149 2017.

150 Somes, C. J., and Oeschler, A.: On the influence of “non-Redfield” dissolved organic
151 nutrient dynamics on the spatial distribution of N₂ fixation and the size of the marine
152 fixed nitrogen inventory, *Global Biogeochemical Cycles*, n/a-n/a,
153 10.1002/2014GB005050, 2015.

154 Weaver, A. J., Eby, M., Wiebe, E. C., Bitz, C. M., Duffy, P. B., Ewen, T. L., Fanning, A.
155 F., Holland, M. M., MacFadyen, A., Matthews, H. D., Meissner, K. J., Saenko, O.,
156 Schmittner, A., Wang, H., and Yoshimori, M.: The UVic earth system climate model:
157 Model description, climatology, and applications to past, present and future climates,
158 *Atmosphere-Ocean*, 39, 361 - 428, 2001.

159